SEMARAK ILMU PUBLISHING

CFD Letters

Journal homepage:
https://semarakilmu.com.my/journals/index.php/CFD_Letters/index
ISSN: 2180-1363

Numerical Study of the Air Outlet Effect Inside a Living Room Connected to an Aerovoltaic Solar Air Heater

Slah Driss[1,*], Ridha Boudhiaf[1], Aram Hmid[1], Ismail Baklouti[1], Abederrahmane Issa[2], Imen Kallel Kammoun[1], Mohamed Salah Abid[1]

[1] Laboratory of Electro-Mechanic Systems (LASEM), National Engineering School of Sfax (ENIS), University of Sfax (USf), B.P. 1173, km 3.5 Soukra, 3038 Sfax, Tunisia
[2] Laboratory of Quantum Physics of Matter and Mathematical Modeling, University of Mascara, Algeria

ARTICLE INFO

Article history:
Received 30 September 2023
Received in revised form 25 October 2023
Accepted 24 November 2023
Available online 31 March 2024

Keywords:
Turbulent flow; aerodynamic structure; CFD; building; design; solar air heater

ABSTRACT

In Sfax–Tunisia, Fossil fuels such as coal, fuel oil and natural gas, are the principle elements responsible for heating of buildings. The problem of pollution result is from the blazing of these fossil fuels and the dramatic increasing in the price of electricity. Thus aerovoltaic solar air heater (ASAH) appears to be a suitable and inexpensive technique for supplying hot air to heat buildings in the sunny area. The idea behind this paper is to employ the ASAH to improve the indoor air quality and thermal comfort by connecting the room and the panel through the use of a pipe. The objective of this work is to develop the design of ASAH and to study numerically the aerodynamic and thermal structures during the heating of a living room connected to an ASAH by means of ANSYS Fluent 17.0.Numerical simulation, implementing a RNG k-ε turbulence model, shows that this technique has a positive effect to improve the thermal comfort in a living room. Thus, it is suggested to employ an ASAH to heat buildings.

1. Introduction

In passive space heating, the buildings are designed or modified so that they independently capture, store, and distribute thermal energy throughout the building without using any electrical or mechanical equipment. Inherently flexible passive solar design principles typically accrue energy benefits with low maintenance risks over the life of the building. The design doesn't need to be complex, but it does involve knowledge of solar geometry, window technology, and local climate. Passive solar heating techniques generally fall into three categories: direct solar gain, indirect solar gain, and isolated solar gain. In this context, Ojike *et al.,* [1] evaluated a passive solar air heater using different storage media. The heater, which is very useful in low temperature applications like drying of agriculture and heating of buildings, is made up of a double-glaze solar thermal collector with a flat plate absorber coupled with thermal storage medium. Kumar *et al.,* [2] studied some low-temperature applications such as room heating, humidifying agent regeneration, and drying of crops

* *Corresponding author.*
E-mail address: slah.driss@gmail.com (Slah Driss)

https://doi.org/10.37934/cfdl.16.8.95120

and industrial items. The incident solar radiation reached the solar air heater was absorbed by the absorber plate and transferred to the air flowing through it. The convective heat transfer coefficient is low between the absorber surface and the flowing air due to the development of laminar sub-layer of air on the absorber surface. Bazri *et al.,* [3] studied a stored latent thermal heat energy. The melted-PCM was used at the supply output hot water using three different phase change materials (PCMs) for the typical high and low solar intensity days. Gaonwe *et al.,* [4] studied the need to reduce energy consumption of hot water production. By maintaining the users thermal comfort level, they developed more energy-efficient technologies. Singh *et al.,* [5] developed a novel approach of coupled CFD-ANN to predict the thermo-hydraulic performance of a solar air heater with rotating circular ribs. Jahangir *et al.,* [6] introduced a novel green HVAC system which reduces both energy consumption and carbon production of buildings. Hassan *et al.,* [7] approuved that the solar air dryers can reduce the large share of energy costs of a final product and can provide sustainable energy in rural areas where access to energy is often limited. Guan *et al.,* [8] studied a heat storage process operated on sunny days. The thermal energy come from a solar air collector. During the heat storage process, the heat storage air valve was opened and the heat release air valve was closed. Gürel [9] developed a temperature-controlled solar air heater (SAH) system with a zigzag finned plate. A flat plate was designed, manufactured, and tested experimentally. Al-Askaree [10] presented a solar water heater with good thermal efficiency, powered only by the sun. Although they seriously harm the environment, oil and gas heaters used in Iraqi homes due to the country's chronic electricity problem. Markam and Maiti [11] studied the typically used air heaters. This system have a low heat transfer coefficient due to the development of a viscous thermal boundary layer near the wall. This fact causes a reduction in the efficiency of the device. The improvement of the heat transfer efficiency can be suitably brought by the passive methods involving artificial enhancers like fin, rib, and groove on the surface near the wall. Saxena *et al.,* [12] studied two models of solar air heater. Their performance analysis have been carried out by comparing them with a reference model. Shetty *et al.,* [13] confirmed that the conventional solar air heaters associated with low thermal are thermohydraulic efficiencies due to the formation of laminar sub-layer created in the region where the flowing air comes in contact with the absorber plate. Yassien *et al.,* [14] developed two triple-pass solar air heater (TPSAH) collectors. They experimentally investigated these collectors to analyse their performances through adding a net of tubes below the absorber surface and double glass cover on one of them for purpose of comparison. Abdallah [15] developed a solar chimney with water heater and phase change material. This system was applied as a passive solar technique for cooling building integrated with short wind tower for low energy building in the hot arid climate. Zhu *et al.,* [16] analyzed the thermal performance of the collector, particularly the temperature distribution in the different localizations of the air collector. The heat loss analysis provided a useful parameter to evaluate the heat loss of the collector. Mazzucco *et al.,* [17] integrated modeling of the MITICA system. Buildings was used to evaluate correctly the overall structural response and carry out all the necessary verifications. Fellin *et al.,* [18] focused on the simulation and verification of the air cooling system of the High Voltage Power Supply. Ifa and Driss [19] studied the evaluation of the thermal sensation for the existing people and examinted the numerical simulation in a room containing a manikin sitting in front of a computer. Bakri *et al.,* [20] studied the impact of the unsteady state of the heat ventilation in a box prototype. The distribution of the velocity fields, the temperature, the total pressure and the turbulent characteristics were studied to characterize the aerodynamic structure of the box prototype. Driss *et al.,* [21] studied the heat ventilation and thermal comfort evaluation in a living room with a patio system. Motte *et al.,* [22] developed specific geometries of the solar heat collector. In comparison with the conventional collector, the side faces are much wider. Its collecting surface generates a specific temperature behavior. Miglioli *et al.,* [23] integrated

photovoltaic-thermal solar heat pump systems to cover the thermal energy needs of buildings, with special emphasis on integration methodologies. The possible configuration was used various sources, and design of sub-system components. Ascione *et al.,* [24] presented the early results of a monitoring campaign. They are shown to characterize the energy performance of this building during the summer season and verify the effectiveness of chosen design solutions. For this reason, the daily energy balance was proposed with the aim to evidence the impact of solar production and electric storage on building energy consumptions. Borrallo-Jiménez *et al.,* [25] studied the passive house standard to warm climates and establishes certain requirements for Heating and Cooling Energy. Cristofari *et al.,* [26] analysed a new flat plate solar collector and a new solar air collector with high building integration. Paraschiv *et al.,* [27] analyzed the integration of renewable energy in the construction sector by using the solar air heating system (SAHS). They evaluated the technico-economic environmental performance of this system to reduce the energy consumption of buildings, economic benefits, and greenhouse gas emissions reduction. Morsy *et al.,* [28] underscores the significance of optimizing indoor environments, particularly in educational buildings, to enhance productivity, satisfaction, and overall sustainability. Focusing on Cairo, Egypt, the study delves into the thermal comfort and energy consumption aspects of educational buildings. Utilizing data from the Egyptian Energy code and simulations from Design Builder software, the research explores the impact of different thermal insulation materials and their thicknesses on the thermal comfort of the building envelope. The methodology combines literature review and computer-based studies to assess the effectiveness of various insulation materials defined in the Egyptian energy code, ultimately aiming to identify the most suitable insulation material. Alawi and Haslinda [29] investigated a flat-plate solar collector (FPSC) using multi-walled carbon nanotubes (MWCNTs), focusing on their impact on temperature and thermal efficiency. MWCNTs with specific characteristics were employed, and a three-dimensional model was analyzed using ANSYS software. Inlet parameters included 1000 W/m² irradiance, a 30°C inlet temperature, and volume flow rates ranging from 0.2 to 0.8 kg/min. The use of MWCNTs decreased the absorber temperature compared to distilled water (DW) across various flow rates. Specifically, at different flow rates, MWCNTs led to temperature reductions of 0.840% to 2.869%, while at the same flow rates, the reductions relative to DW ranged from 0.633% to 0.874%. Additionally, the thermal efficiency of the MWCNTs nanofluid increased by 6.080% to 6.857% across the specified volume flow rates. Samsudin *et al.,* [30] discussed the current reliance on fossil fuels, particularly coal, natural gas, and fuel oil, for power generation in Malaysia. Highlighting the environmental impact and finite nature of these resources, the author emphasized the need for alternative fuels to sustain power generation as Malaysia aims to become a high-income nation.

The luck of research in the above literature is that there is no experimental and numerical study available to analyze the aerodynamic and thermal structures in a living room connected to an aerovoltaic solar air heater under the climate of Sfax region central-eastern Tunisia. Novelty of this numerical simulation lies specifically in the case study of living room connected to an aerovoltaic solar air heater under climatic conditions of Sfax region central-eastern Tunisia and to evaluate the potential of this technology in this region of the world. In the present work, simulations are done by employing ANSYS Fluent 17.0 CFD computational fluid dynamics techniques under climatic conditions of Sfax, Tunisia and obtained numerical results have validated with an experimental work. In addition, numerical results represent the Sfax region, because there is a large potential for the construction of aerovoltaic solar air heater connected to a living room in this location.

The objective of the present work is to study the effect of air outlet in the aerodynamic and thermal structure inside a living room connected to air voltaic solar air heater.

2. Geometric Parameters

By referring to a living room which already exist in the region of Sfax Tunisia, we are referred to the building presented in Figure 1. In this building, the living room presents a height h = 2.55 m, a width w = 4 m and a length l = 5 m. Figure 2 shows the geometrical parameters and the boundary conditions of the considered numerical model. The room walls are made of the standard brick. The air-outlet's diameter is defined by Ds and the distance between the wall and the air-outlet's center equal to Dc = 0.4 m. The channel domain and the collector have the same width which are equal to W=0.952 m and a total length equal to Lp = 1.585 m. The length of the collector is Lc=0.18 m and the thickness of the panel area is equal to e=0.04 m. The panel is oriented towards the south and the slope is equal to β= 30°. This room correspond on a practical case study located in Sax city. This choice was adopted to investigate the aero thermal characteristics of the considered living room.

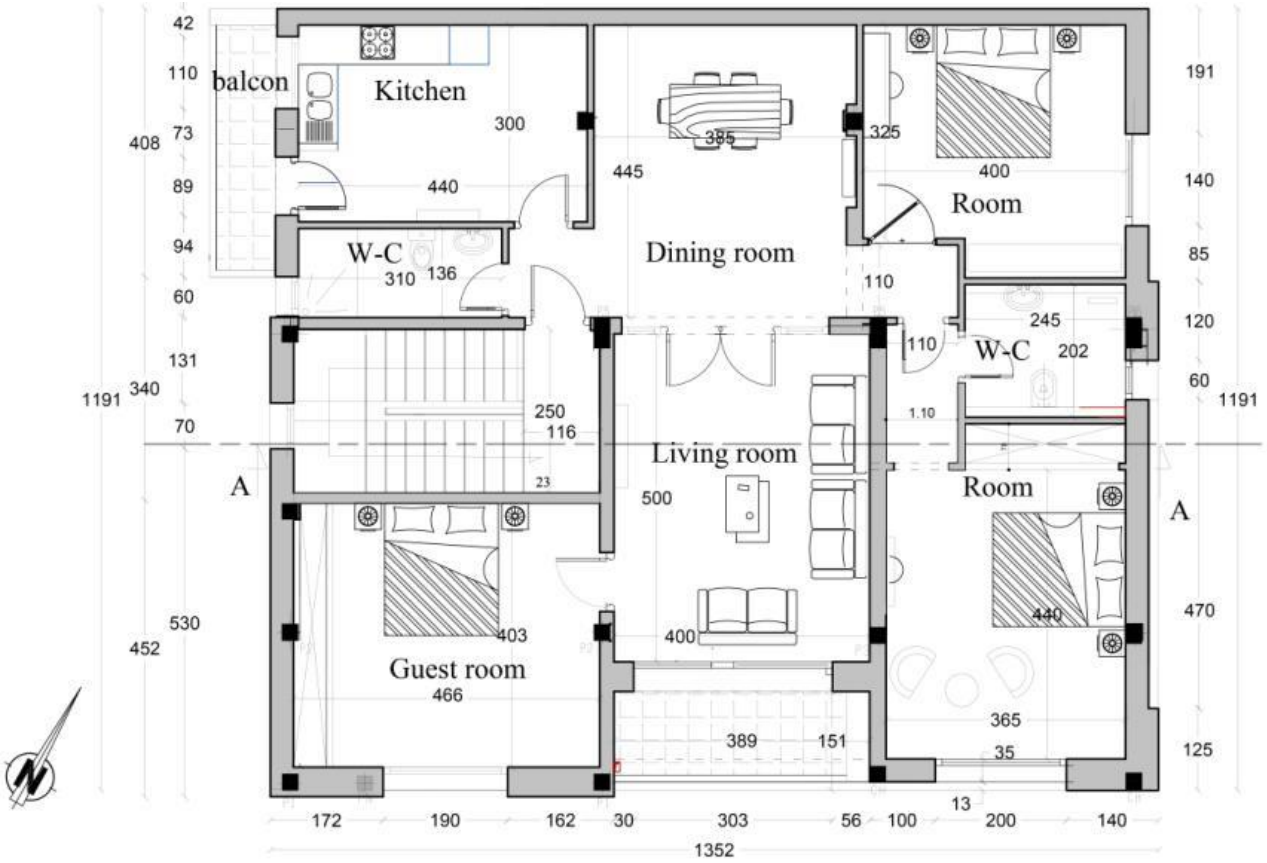

Fig. 1. Building plan

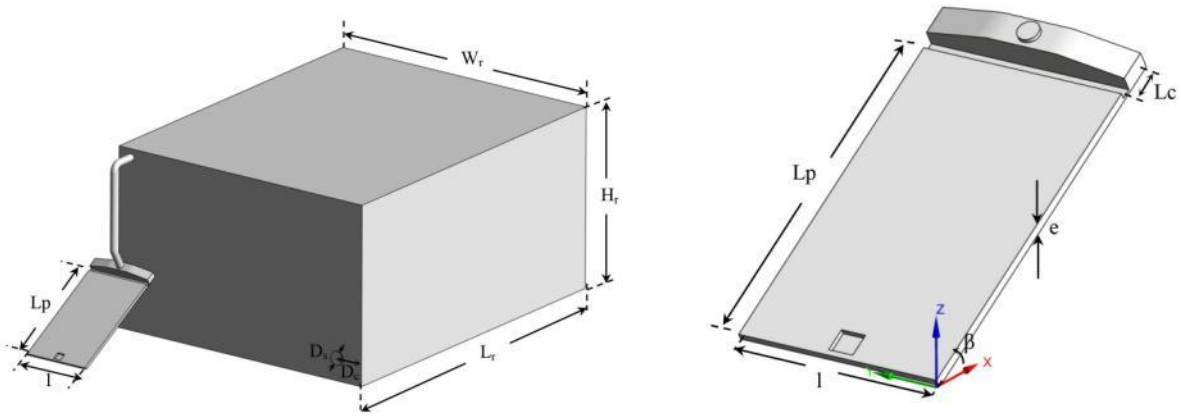

(a) (b)

Fig. 2. Geometrical arrangement (a) Living room (b) Solar panel

3. Numerical Model

3.1 Mathematical Formulation

ANSYS Fluent employs the fundamental three-dimensional fluid mechanic equations for conservation of mass, momentum, and energy to calculate fluid properties. The continuity equation expresses the law of conservation of mass for a given volume control:

$$\frac{d\rho}{dt}+\vec{\nabla}.(\rho\vec{V})=0 \tag{1}$$

Where ρ is the density, t is the time and $\vec{V}$ is the velocity vector.

For the incompressible fluids, the continuity equation can be written as follows:

$$\frac{\partial}{\partial x_i}(\rho u_i)=0 \tag{2}$$

The momentum equations are written as follows:

$$\frac{d\,\rho\vec{V}}{dt} + \left(\rho\vec{V}.\vec{\nabla}\right).\vec{V}= -\vec{\nabla}p + \vec{\nabla}.\bar{\bar{\tau}} + \rho.\vec{g} \tag{3}$$

Where p is the static pressure, ρ is the density, t is the time and $\vec{V}$ is the velocity vector.

The stress tensor $\bar{\bar{\tau}}$ is expressed as:

$$\bar{\bar{\tau}} = 2\,\mu\,\bar{\bar{D}} - \vartheta\,(\vec{\nabla}.\vec{V}).\bar{\bar{I}} \tag{4}$$

Where:

$$\bar{\bar{D}}= \frac{1}{2}(\bar{\bar{\nabla}}.\vec{V} + \bar{\bar{\nabla}}^t.\vec{V}) \tag{5}$$

Thus:

$$\bar{\bar{\tau}} = \mu((\bar{\bar{\nabla}}.\vec{V} + \bar{\bar{\nabla}}^t.\vec{V}) - \frac{2}{3}(\vec{\nabla}.\vec{V})\bar{\bar{I}}) \quad (6)$$

Where $\bar{\bar{I}}$ is the identity matrix and μ is the dynamic viscosity.

Basing on the first principle of thermodynamics, we can express the conservation equation of energy. This principle connects the various forms of energy, that is to say:

$$\frac{d(\rho E)}{dt} + \vec{\nabla}(\rho E\vec{V}) = \vec{\nabla}(\bar{\bar{\tau}}\vec{V}) + \rho\vec{f}\vec{V} - \vec{\nabla}\vec{q} - \vec{\nabla}p\vec{V} + r \quad (7)$$

Where E is the total internal energy in the system, and r is the additional energy source term

The enthalpy h of the fluid is expressed as:

$$h = \int C_p dT \quad (8)$$

Where C_p is the constant pressure specific heat. Then, the energy equation can be written as follows:

$$\frac{\partial}{\partial x_j}(\rho C_p u_j T) = \frac{\partial}{\partial x_j}\left(k\frac{\partial T}{\partial x_j}\right) + \tau_{ij}\frac{\partial u_i}{\partial x_j} + \beta T\left(u_j\frac{\partial p}{\partial x_j}\right) \quad (9)$$

To build precisely our models, it is necessary to take account of simplifying assumptions. For that, we consider that the fluid is Newtonian and incompressible flow. Thus, the stress tensor is proportional to the symmetrical part of the tensor of the rates of deformation. The stress tensor can be reduced to:

$$\bar{\bar{\tau}} = \mu(\bar{\bar{\nabla}}\vec{V}) \quad (10)$$

When the total conductivity is constant, the heat flow is proportional to the gradient of the temperature:

$$\vec{q} = -\lambda\vec{\nabla}T \quad (11)$$

The total conductivity λ takes into account the thermal conductivity of the fluid and the turbulent thermal conductivity.
The viscous dissipation flow of the heat is negligible which results in the equation according to:

$$\vec{\nabla}.(\bar{\bar{\tau}}.\vec{v}) \ll |\vec{\nabla}.\vec{q}| \quad (12)$$

Boussinesq model can be assumed for the buoyancy force in the momentum equation that the density varies only linearly with the temperature:

$$\rho = \rho_0[1 - \beta(T - T_0)] \quad (13)$$

Where β is the thermal expansion coefficient defined as follows:

$$\beta=-1/\rho\left(\frac{d\rho}{dT}\right) \tag{14}$$

3.2 Turbulent Models

The k-ε model is one of the most common turbulence models, although it just does not perform well in cases of large adverse pressure gradients. It is a two-equation model and includes two extra transport equations to represent the turbulent properties of the flow. This allows a two equation model to account for history effects like convection and diffusion of turbulent energy. The first transported variable is the turbulent kinetic energy k. The second transported variable in this case is the dissipation rate of the turbulent kinetic energy ε. It is the variable that determines the scale of the turbulence, whereas the first variable k determines the turbulent kinetic energy.

The RNG k-ε model was derived using a statistical technique called renormalization group theory. It is similar in form to the standard k-ε model, but includes the following refinements:

i. The RNG turbulence model has an additional term in its ε equation that improves the accuracy for rapidly strained flows.
ii. The effect of swirl on turbulence is included in the RNG turbulence model, enhancing accuracy for swirling flows.
iii. The RNG theory provides an analytical formula for turbulent Prandtl numbers, while the standard k-ε model uses user-specified, constant values. While the standard k-ε model is a high-Reynolds number model, the RNG theory provides an analytically derived differential formula for effective viscosity that accounts for low-Reynolds number effects. Effective use of this feature does, however, depend on an appropriate treatment of the near-wall region. These features make the RNG k-ε model more accurate and reliable for a wider class of flows than the standard k-ε model. The RNG-based k-ε turbulence model is derived from the instantaneous Navier-Stokes equations, using a mathematical technique called "renormalization group" (RNG) methods. The analytical derivation results in a model with constants different from those in the standard k-ε model, and additional terms and functions in the transport equations for k and ε are written as follows:

$$\frac{\partial}{\partial t}(\rho k)+\frac{\partial}{\partial x_i}(\rho k u_i)=\frac{\partial}{\partial x_j}\left(\alpha_k \mu_{eff}\frac{\partial k}{\partial x_j}\right)+G_k+G_b-\rho\varepsilon-Y_M+S_k \tag{15}$$

$$\frac{\partial}{\partial t}(\rho \varepsilon)+\frac{\partial}{\partial x_i}(\rho \varepsilon u_i)=\frac{\partial}{\partial x_j}\left(\alpha_\varepsilon \mu_{eff}\frac{\partial \varepsilon}{\partial x_j}\right)+\frac{\varepsilon}{k}C_{1\varepsilon}(G_k+C_{3\varepsilon}G_b)-C_{2\varepsilon}\rho\frac{\varepsilon^2}{k}-R_\varepsilon+S_\varepsilon \tag{16}$$

Where G_k is the generation of turbulence kinetic energy due to the mean velocity gradient, G_b is the generation of turbulence kinetic energy due to buoyancy, and Y_M is the contribution of the fluctuating dilatation in compressible turbulence to the overall dissipation rate.
The quantities α_k and α_ε are the inverse effective Prandtl numbers for k and ε, respectively.

S_k and S_ε are the user-defined source terms. The scale elimination procedure in RNG theory results in a differential equation for turbulent viscosity:

$$d\left(\frac{\rho^2 k}{\sqrt{\mu\varepsilon}}\right)=1.72\frac{\hat{V}}{\sqrt{\hat{V}^3-1+C_V}}d\hat{V} \tag{17}$$

Where:

$$\widehat{V} = \frac{\mu_{eff}}{\mu} \tag{18}$$

$$C_V \approx 100 \tag{19}$$

Eq. (19) is integrated to obtain an accurate description of how the effective turbulent transport varies with the effective Reynolds number, allowing the model to better handle low-Reynolds-number and near-wall flows. In the high-Reynolds-number limit, the turbulent viscosity is written as follows:

$$\mu_t = \rho C_\mu \frac{k^2}{\varepsilon} \tag{20}$$

Where C_μ =0.0845 is derived using the RNG theory.

It is interesting to note that this value of C_μ is very close to the empirically determined value of 0.09 used in the standard k-ε model. In general, turbulence is affected by rotation or swirl in the mean flow. The RNG model provides an option to account the effects of swirl or rotation by modifying the turbulent viscosity appropriately. The modification takes the following function at form:

$$\mu_t = \mu_{t0}\, f(\, \alpha_s, \Omega, \frac{k}{\varepsilon}) \tag{21}$$

Where μ_{t0} is the value of turbulent viscosity calculated without the swirl modification using either Eq. (18) or Eq. (20).

Ω is a characteristic swirl number evaluated.

3.3 Surface-to-Surface (S2S) Radiation Model Theory

The surface-to-surface radiation model can be used to account for the radiation exchange in an enclosure of gray-diffuse surfaces. The energy exchange between two surfaces depends in part on their size, separation distance, and orientation. These parameters are accounted by a geometric function called a “view factor”. The main assumption of the S2S model is that any absorption, emission, or scattering of radiation can be ignored. Therefore, only “surface-to-surface” radiation need to be considered for analysis. The energy flux leaving a given surface is composed of directly emitted and reflected energy. The reflected energy flux is dependent on the incident energy flux from the surroundings, which then can be expressed in terms of the energy flux leaving all other surfaces. The energy eaving from surface k is:

$$q_{o,k}=\varepsilon_k \sigma T_k^4 + \rho_k q_{in,k} \tag{22}$$

Where $q_{o,k}$ is the energy flux leaving the surface, ε_k is he emissivity, σ is the Stefan-Boltzmann constant, and $q_{in,k}$ is the energy flux incident on the surface from the surroundings.

The amount of incident energy upon a surface from another surface is a direct function of the surface to surface “view factor”F_{jk}. The view factor F_{jk} is the fraction of energy leaving surface that is

incident on surface. The surfaces used in the calculation of a view factor can be mesh faces or clusters of faces (for 3D cases only). The incident energy flux $q_{in,k}$ can be expressed in terms of the energy flux leaving all other surfaces as:

$$A_k q_{in,k} = \sum_{j=1}^{N} A_j \, q_{out,j} F_{jk} \quad (23)$$

Where A_k is the area of surface k and F_{jk} is the view factor between surface k and surface j.

3.4 Boundary Conditions

Figure 3 and Table 1 presents the location of the boundary conditions on the computational domain. The ambient air temperature values are taken from the experimental measures in each case of simulation as well as the overall air input-output temperature and the temperature of the overall cells. Indeed, the inlet condition is defined by the atmospheric pressure inlet. Also, the output surface of the domain is affected by the exhaust-fan condition with a specific mass flow target. The radiation surface condition is taken by surface-to-surface radiation model (S2S). Although, the remaining walls are assumed adiabatic. Figure 4 shows the control zone of the aero-thermal domain and their specifical air channel dimensions. Precisely, the air domain under the aerovoltaic solar air heater panel comprises limited by the lower surface of the Tedlar layer and the insulating surface.

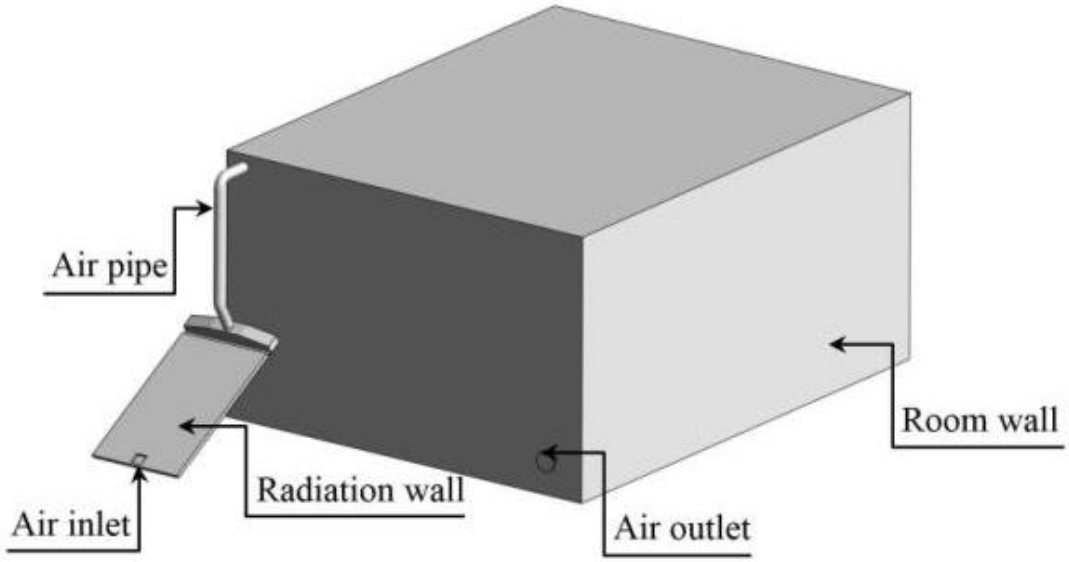

Fig. 3. Boundary conditions

Table 1
Boundary condition

Boundary conditions	Air-inlet temperature T_{in} (K)	Air-Outlet temperature T_{out} (K)	Global solar radiation G ($W.m^2$)	Mass flow $\dot{m}$ ($Kg.s^{-1}$)	Gravity g ($m.s^{-2}$)
Values	298	320	1031	0.02	9.81

4. Comparison with Experimental Results

Figure 4 presents the mesh size effects on the CFD results due to the difference of the number of elements and nodes from a configuration to another. The number of nodes and elements must be

enough to solve the geometry. In fact, the relevance of the choice of meshing is based on the number of nodes suitable for the convergence of the CFD model, the structure type such as quadratic type and the minimum calculation time. Four simulations were done to evaluate the optimum node size and elements. Figure 5 shows the different CFD meshing sizes, with different fragments. The meshing characteristics with the calculation time are presented in Table 2. The comparison of the experimental and the numerical results are assigned to the simulation of the temperature profiles. The choice of the suitable meshing is deduced by the comparison with the experimental values. Our choice is based on the minimum error and the minimum computational time. Figure 6 shows the temperature profile in the line L_1 defined by x=0.216 m and z=0.02 m. These profiles present the same appearance and shows the symmetry according to the width of the panel with a significant temperature peak in the middle respectively equal to T=302 K, T=312 K and T=320 K as well as in the border T=310 K, T=318 K and T=324 K. The collector geometry affects a variety in the distribution while the fan effect presents a temperature decrease in the middle point with a value equal to T=321 K. From these results, it is clear that the configuration with 460 000 nodes is more adequate to be considered for our numerical simulation.

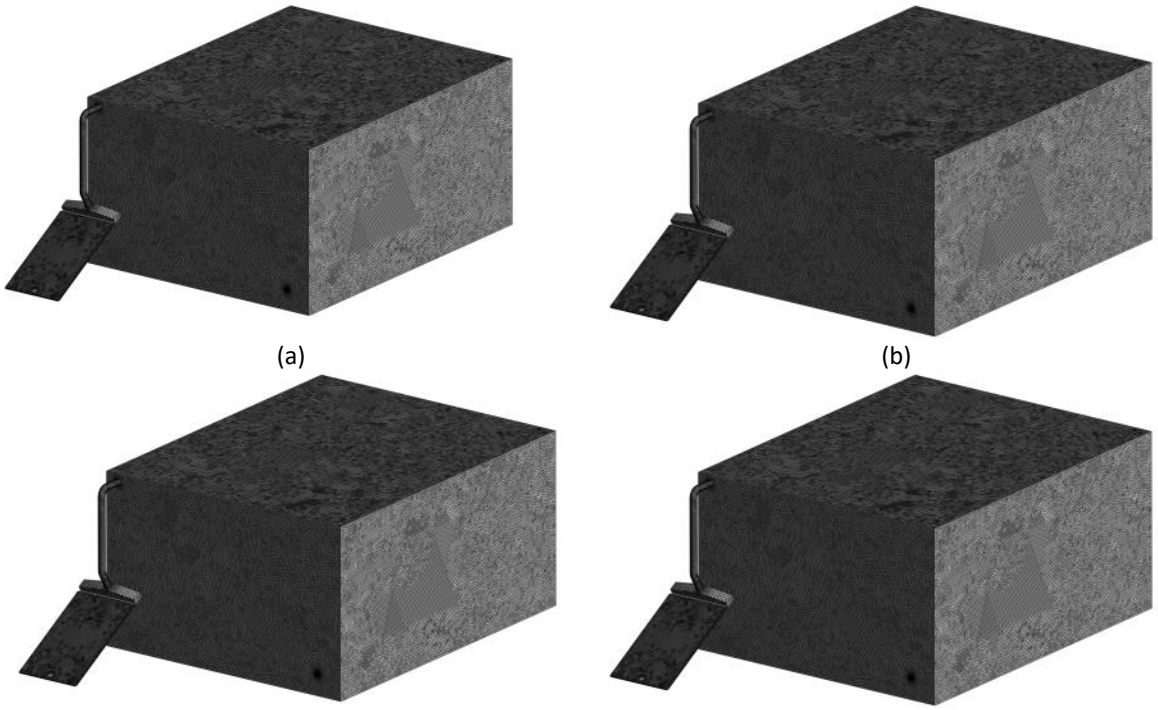

(a) (b) (c) (d)

Fig. 4. Meshing (a) D_s = 5 cm (b) D_s = 10 cm (c) D_s = 15 cm (d) D_s = 20 cm

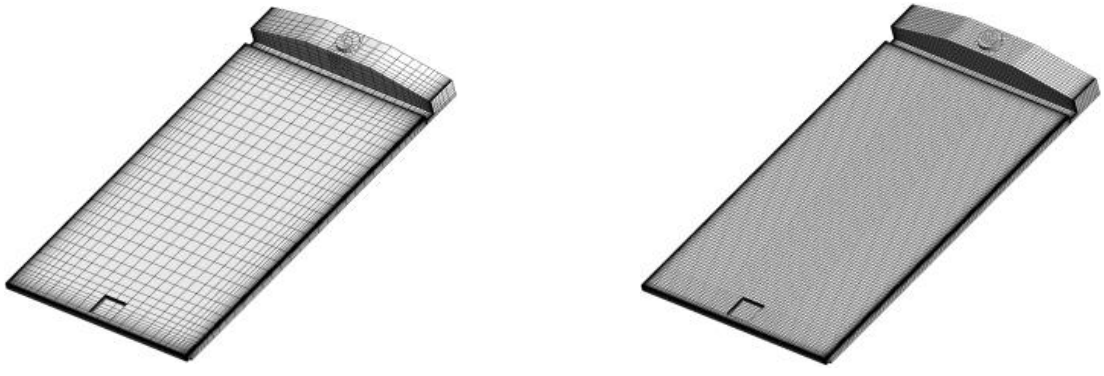

(a) (b)

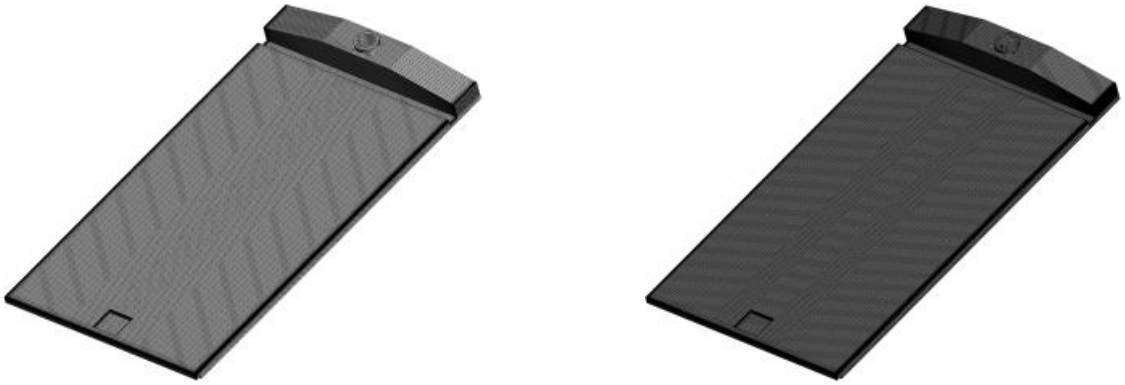

(c) (d)

Fig. 5. CFD meshing sizes (a) 35000 nodes (b) 141000 nodes (c) 500000 nodes (d) 1100000 nodes

Table 2
Meshing characteristics with the calculation time

Nodes number	Element size (m)	Calculation time (h: min: s)	Iterations number
35000	0.05	5:05:11	100000
140000	0.015	6:33:18	100000
450000	0.0075	24:59:51	100000
1150000	0.005	72:12:18	100000

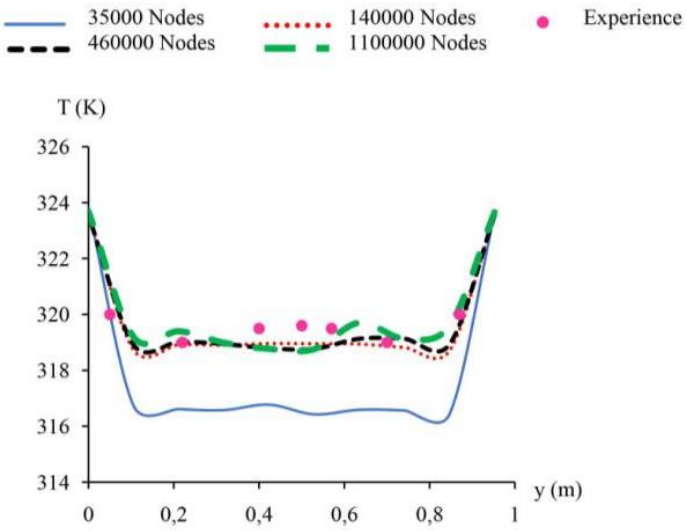

Fig. 6. Temperature profiles in the direction defined by z=0.02 m and x= 1.216 m

5. Numerical Results

The considered planes of the local characteristics are shown in Figure 7. The panel coordinates system (x, y, z) is preserved and another coordinates system (X, Y, Z) is established for the room.

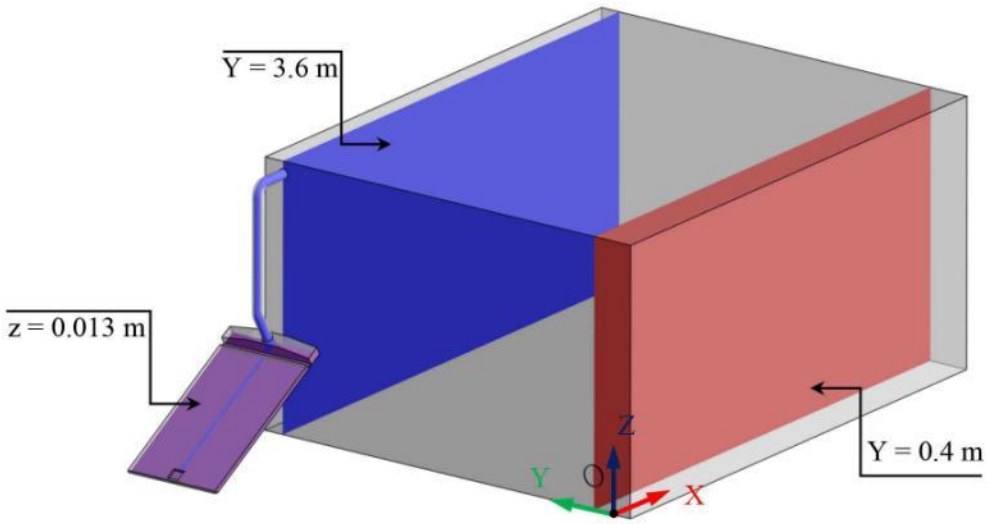

Fig. 7. Considered planes

5.1 Temperature

Figures 8, 9 and 10 display the temperature distribution in the considered planes defined by z = 0.013 m, Y = 0.4 m and Y = 3.6 m. The first plane defined by z = 0.013 m is considered inside the panel. The second plane defined by Y = 3.6 m pass through the panel and the air pipe. The third plane defined by Y = 0.04 m pass through the air-outlet. From these results, the collector shows a uniform distribution across the geometrical system with a temperature peak just before the collector with a value equal to T = 302K. Inside the room walls, it has been noted a uniformity in the temperature distribution with a maximum temperature at the connection point between the air pipe and the room wall with a value equal to T = 301 K. In these conditions, the temperature decreases to T = 299 K in most of the room space. The temperature doesn't change much, and it'is mostly fixed at T = 299 K. By comparring the different configurations, the air temperature presents similar distrubution throughout the room space. After the air passes throught the aerovoltaic panel, the air temperature inside the air pipe decreases from T = 308 K to T = 299 K. This temperature remains fixed until the air reaches the room and spreads inside the room space. Indeed, it has been confirmed that the air-outlet diameter has no major effect on the temperature of the room, which can be explained by the difference between the size of the air-outlet and the size of the fluid domain.

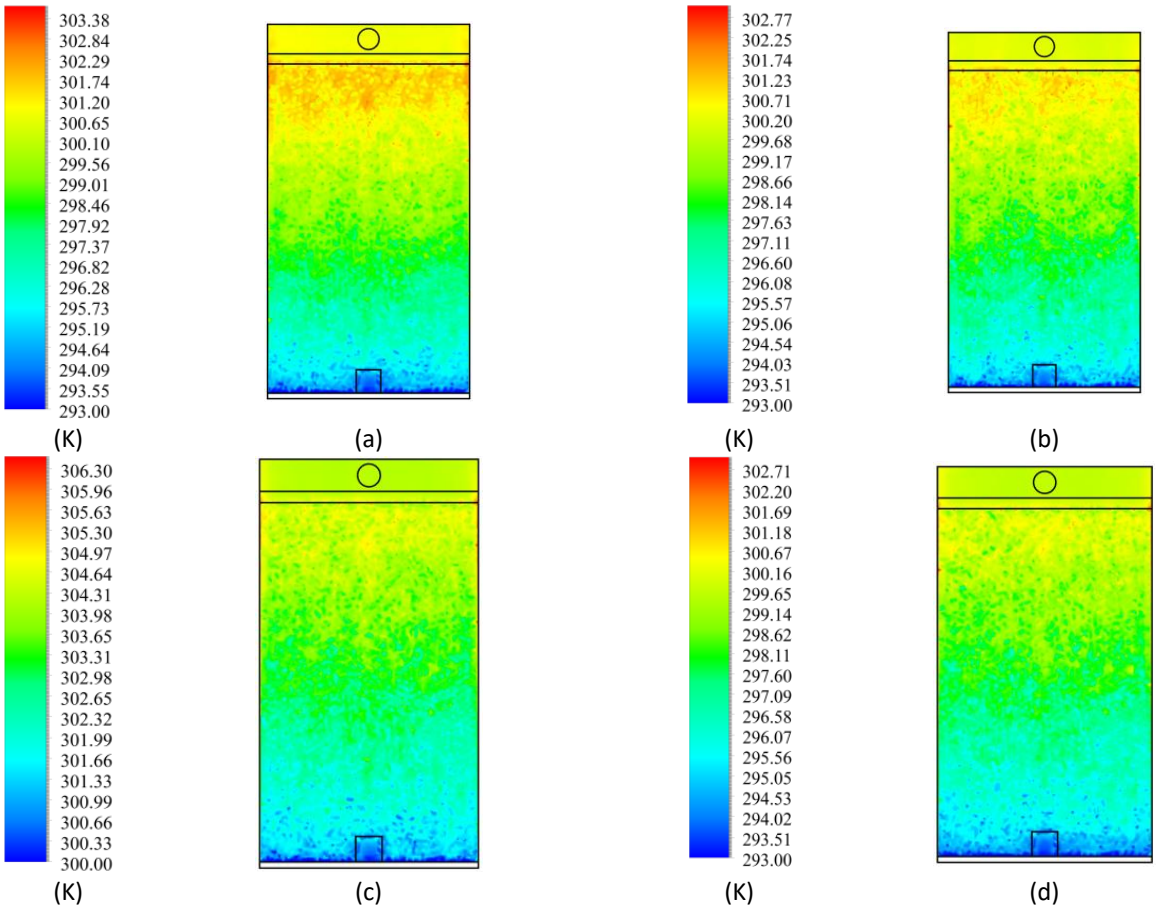

Fig. 8. Temperature distribution in the plane defined by z= 0.013 m (a) D_s= 5 cm (b) D_s =10 cm (c) D_s =15 cm (d) D_s =20 cm

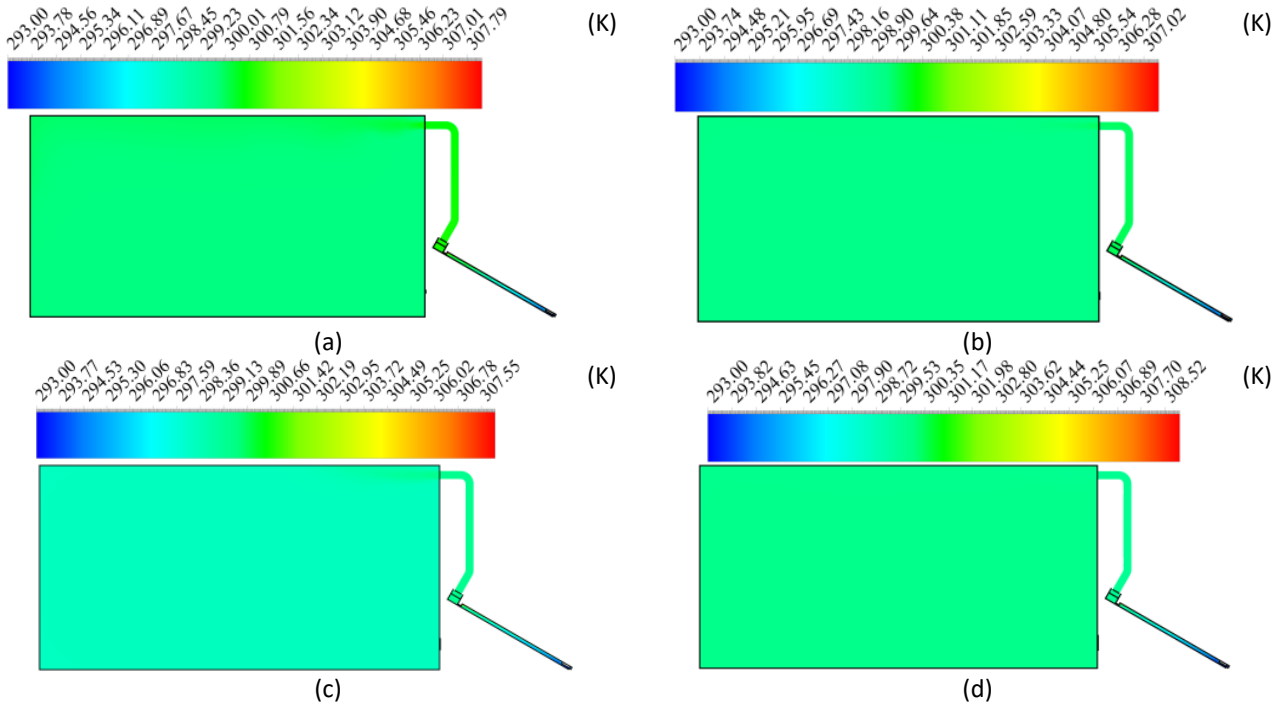

Fig. 9. Temperature distribution in the plane defined by Y =3.6 m (a) D_s= 5 cm (b) D_s = 10 cm (c) D_s= 15 m (d) D_s= 20 cm

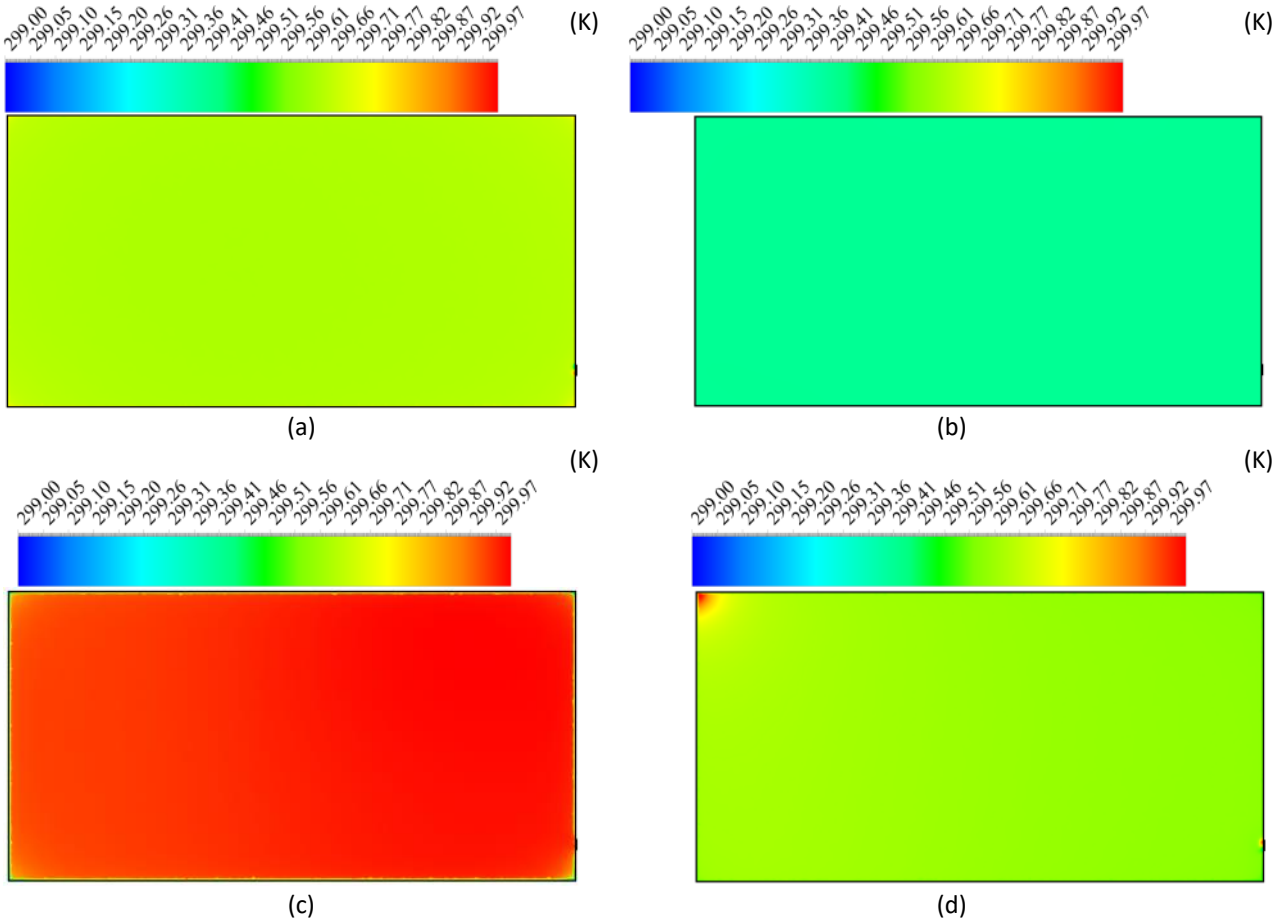

Fig. 10. Temperature distribution in the plane defined by Y = 0.4 m (a) D_s = 5 cm (b) D_s= 10 cm (c) D_s = 15 cm (d) D_s = 20 cm

5.2 Velocity Fields

Figures 11, 12 and 13 present the velocity variation for different diameters outlet equal to Ds=5 cm, Ds=10 cm, Ds=15 cm, and Ds=20 cm. These planes are defined by z = 0.013 m, Y = 0.4 m and Y = 3.6 m have been considered. The first plane defined by z = 0.013 m is considered inside the panel. The second plane defined by Y = 3.6 m pass through the panel and the air pipe. The third plane defined by Y = 0.04 m pass through the air-outlet. According to these results, it is clear that the velocity distribution is uniform in the air domain of panel. Inside the collector, an acceleration zone appears due to the reduction of the geometry. Inside the panel, the velocity presents a maximum value equal to 1.4 $m.s^{-1}$. Via the pipe separating the aerovoltaic panel from the room, a discharge area appears in the inlet hole and invaded the reverse wall. At this level, the velocity changes its direction and two axial flows have been observed. The first ascending flow is responsible on the recirculation zone appearing in the whole area of the room. This movement continues until the exit of the air flow through the air-outlet and reaches the maximum value equal to V= 3 $m.s^{-1}$. The second descending flow is due to the dead zone appeared in the down area. Globally, the averaged velocity value is about V=1.5 $m.s^{-1}$ in the discharge area.

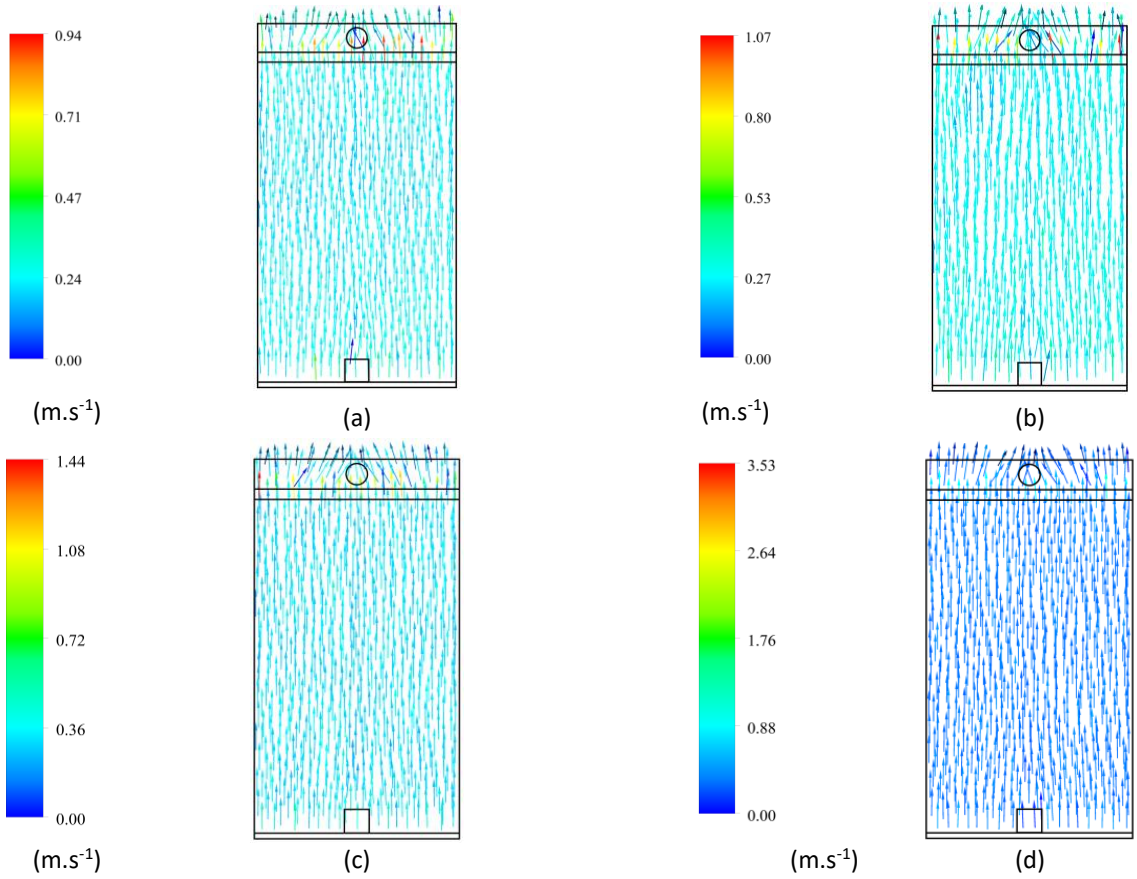

Fig. 11. Velocity fields in the plane defined by z = 0.013m (a) D_s =5 cm (b) D_s= 10 cm (c) D_s= 15 cm (d) D_s= 20 cm

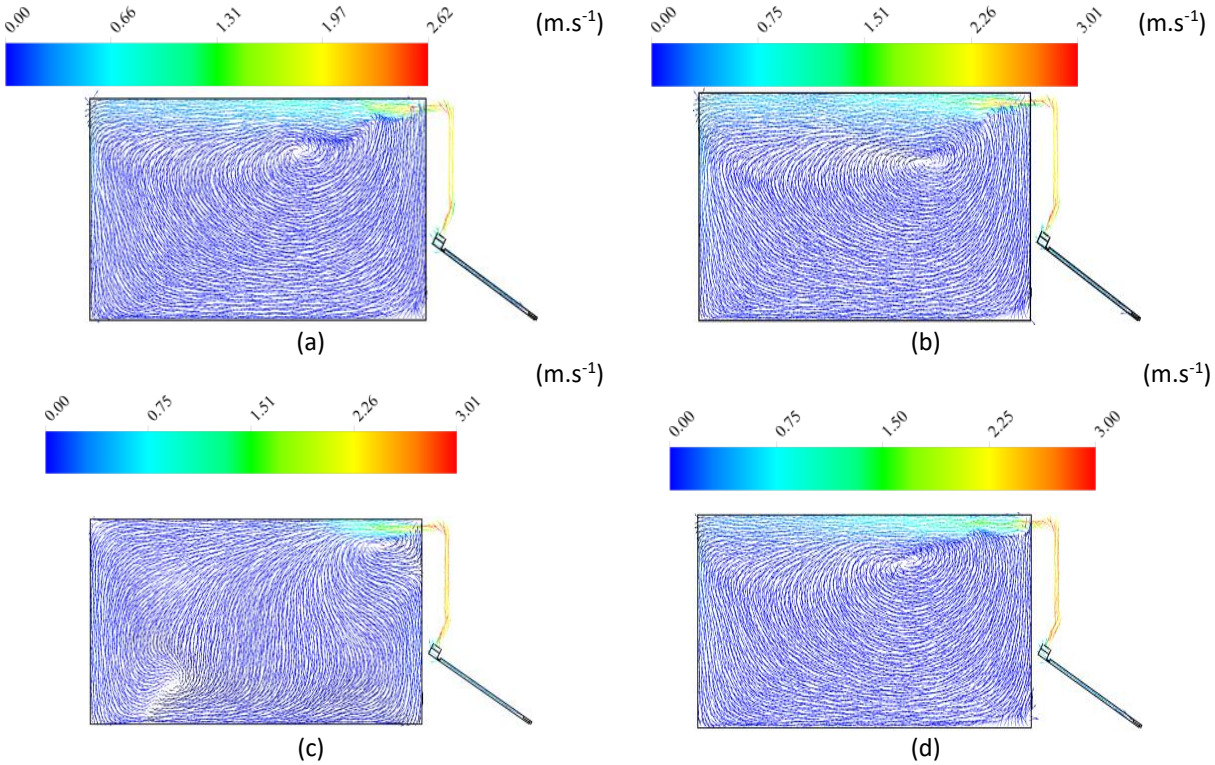

Fig. 12. Velocity fields in the plane defined by Y = 3.6 m (a) D_s= 5 cm (b) D_s = 10 cm (c) D_s =15 cm (d) D_s= 20 cm

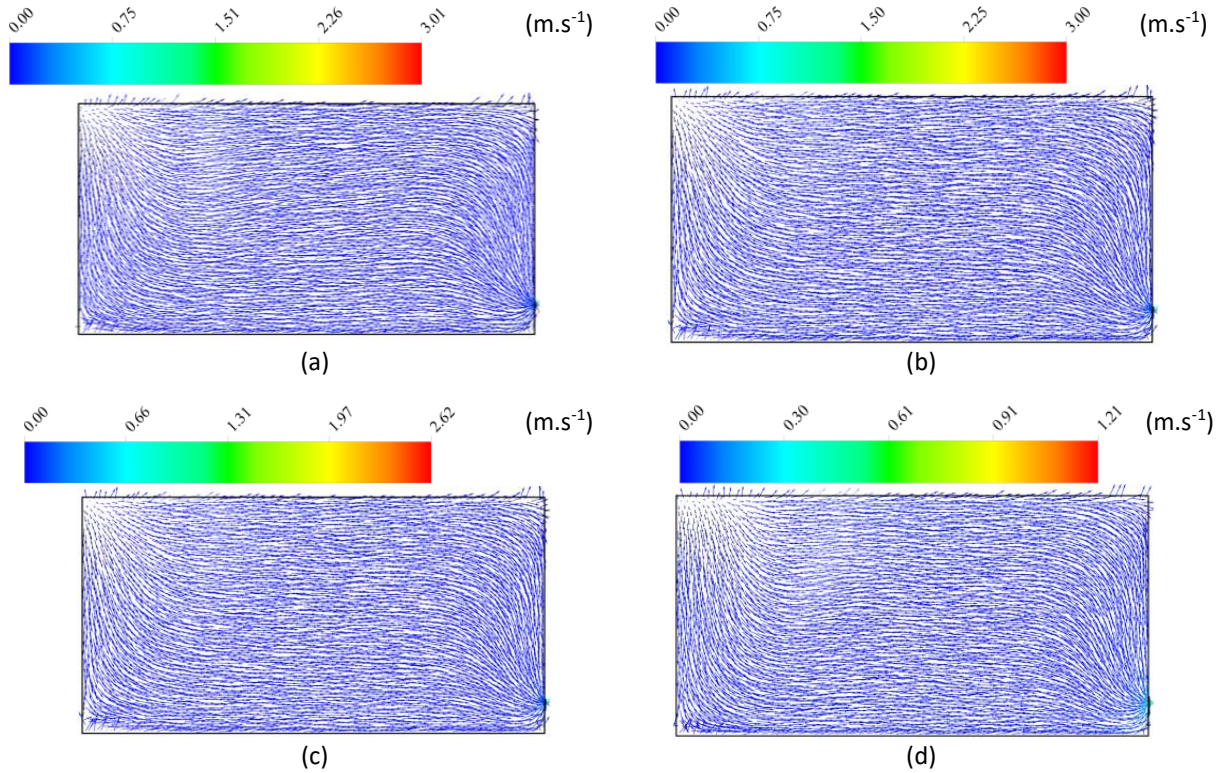

Fig. 13. Velocity fields in the plane defined by Y = 0.4 m (a) D_s = 5 cm (b) D_s = 10 cm (c) D_s = 15 cm (d) D_s = 20 cm

5.3 Static Pressure

The distribution of the static pressure in the whole volume of the aerovoltaique panel is depicted in Figures 14, 15 and 16 for the different considered planes defined by z = 0.013 m, Y = 0.4 m and Y = 3.6 m. The first plane defined by z = 0.013 m is considered inside the panel. The second plane defined by Y = 3.6 m pass through the panel and the air pipe. The third plane defined by Y = 0.04 m pass through the air-outlet. According to these results, the static pressure distributions are not uniform under the panel. Through the panel, the static pressure distribution varies according to the air-outlet's diameter with a maximum value of p = 1.86 Pa. Inside the room, the static pressure distribution varies across the different geometrical system with a maximum value of p = 346 Pa. Through the air advancement, the total pressure decreases quietly in the expulsion area, produced from the air-inlet and through the room wall. This fact can be explained by the recirculation zone appeared in the wholes area of the room. In the air-outlet, a depression zone characteristic of the minimum value, equal to P = -8 Pa, has been observed. The comparison between the results confirms that the maximum value of the pressure equal to p= 100 Pa is obtained for the configuration defined by D_s= 5. However, the minimum value of the pressure equal to p=-50 Pa is obtained for the configuration defined by D_s=20 cm. According to these results, it has been observe a non-uniform distribution of pressure inside the panel. This fact is due to the decrease of the collector area relating the panel with living room.

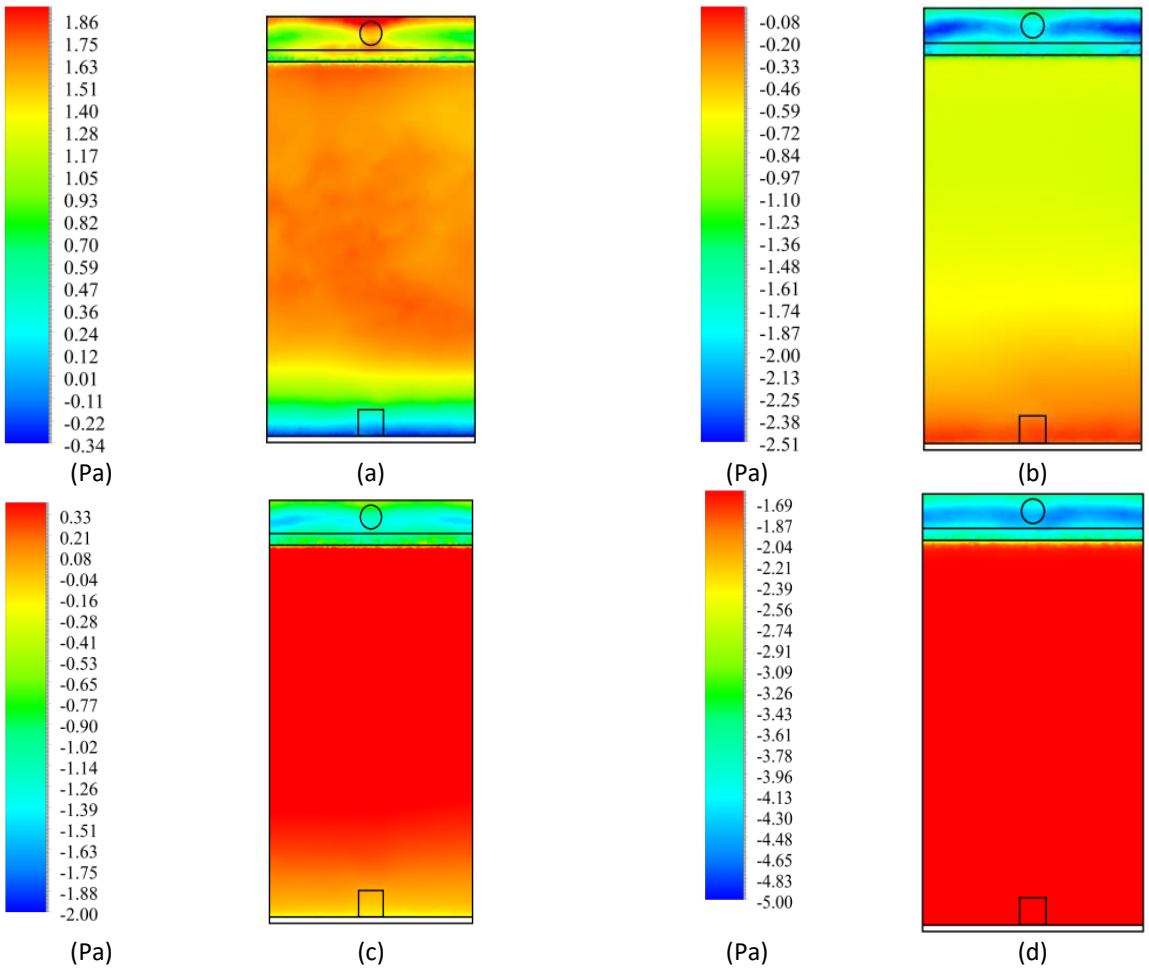

Fig. 14. Static pressure distribution in the plane defined by z = 0.013 m (a) D_s = 5 cm (b) D_s = 10 cm (c) D_s = 15 cm (d) D_s = 20 cm

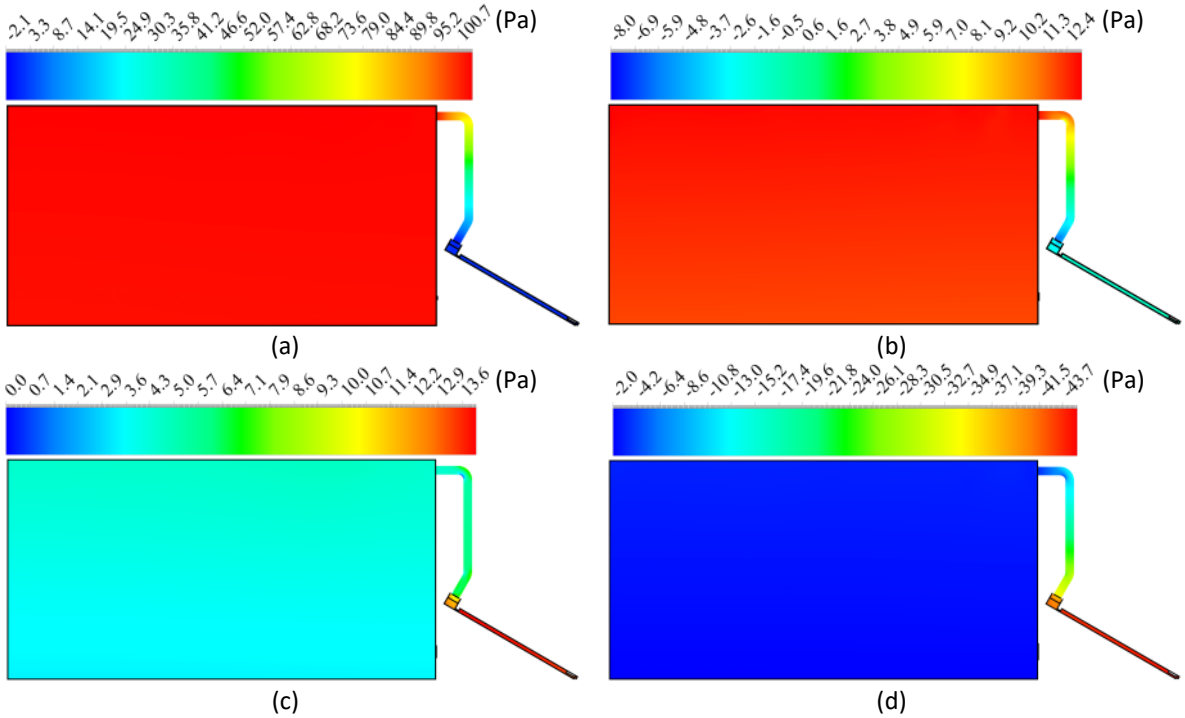

Fig. 15. Static pressure distribution in the plane defined by Y = 3.6 m (a) D_s = 5 cm (b) D_s = 10 cm (c) D_s = 15 cm (d) D_s = 20 cm

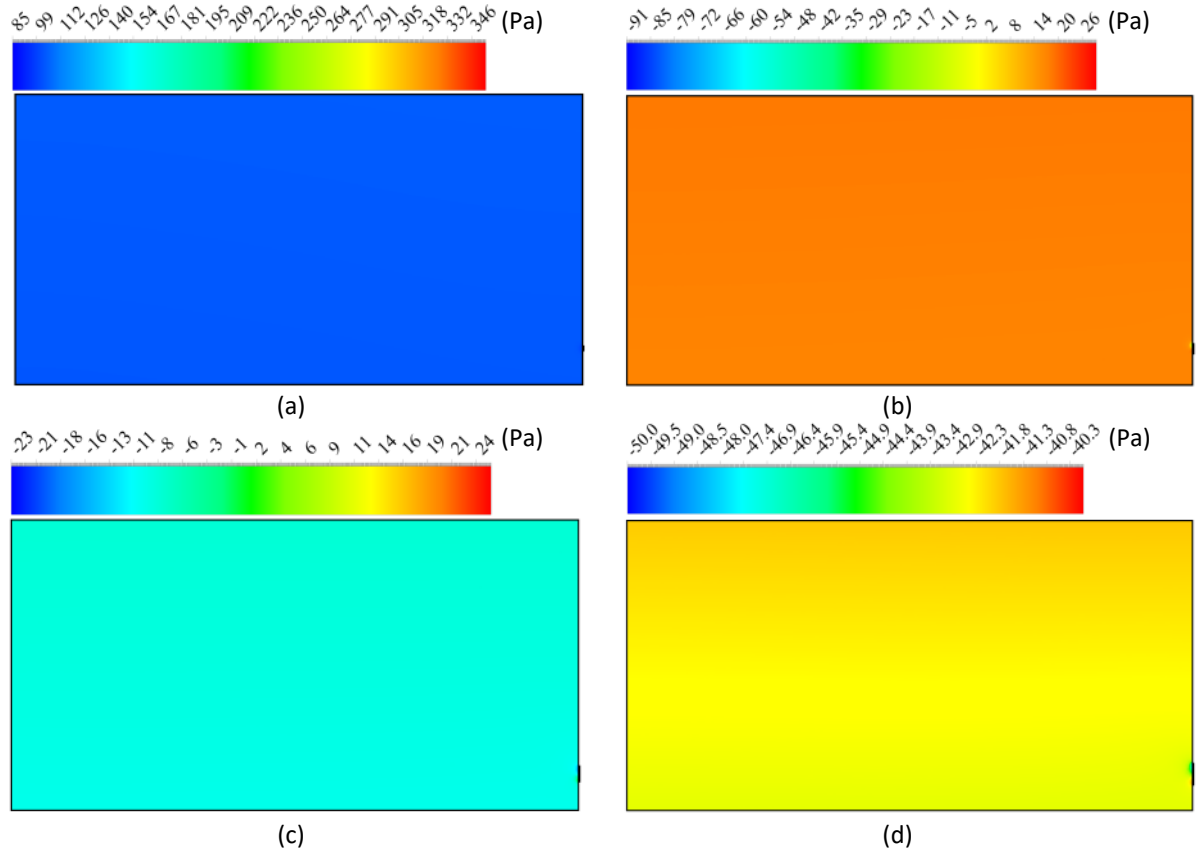

Fig. 16. Static pressure distribution in the plane plane defined by Y = 0.4 m (a) D_s = 5 cm (b) D_s = 10 cm (c) D_s = 15 cm (d) D_s = 20 cm

5.4 Turbulent Kinetic Energy

Figures 17, 18 and 19 show the distribution of the turbulent kinetic energy for the different considered planes defined by z = 0.013 m, Y = 0.4 m and Y = 3.6 m for different diameters outlet equal to D_s = 5 cm, D_s = 10 cm, D_s = 15 cm, and D_s = 20 cm. According to these results, the wake zone characteristic of the maximum value of the turbulent kinetic energy is the same for the different cases. It appears in the collector air channel with an uniformity inside the panel air domain. However, the minimum values are located in the panel air volume. Inside the room, the turbulent kinetic energy distribution varies across the different geometrical system with a maximum value of k = 0.305 J.kg^{-1}. After the decrease of the turbulent kinetic energy in the second part of the pipe, an expulsion area appears in the air inlet of the room and is invaded in the discharge area until the room wall. The comparison between the results confirms that the maximum value of the turbulent kinetic energy equal to k= 97J.kg^{-1} is obtained for the configuration defined by D_s= 5. However, the minimum value of the turbulent kinetic energy equal to k=0.016 J.kg^{-1} is obtained for the configuration defined by D_s=20 cm.

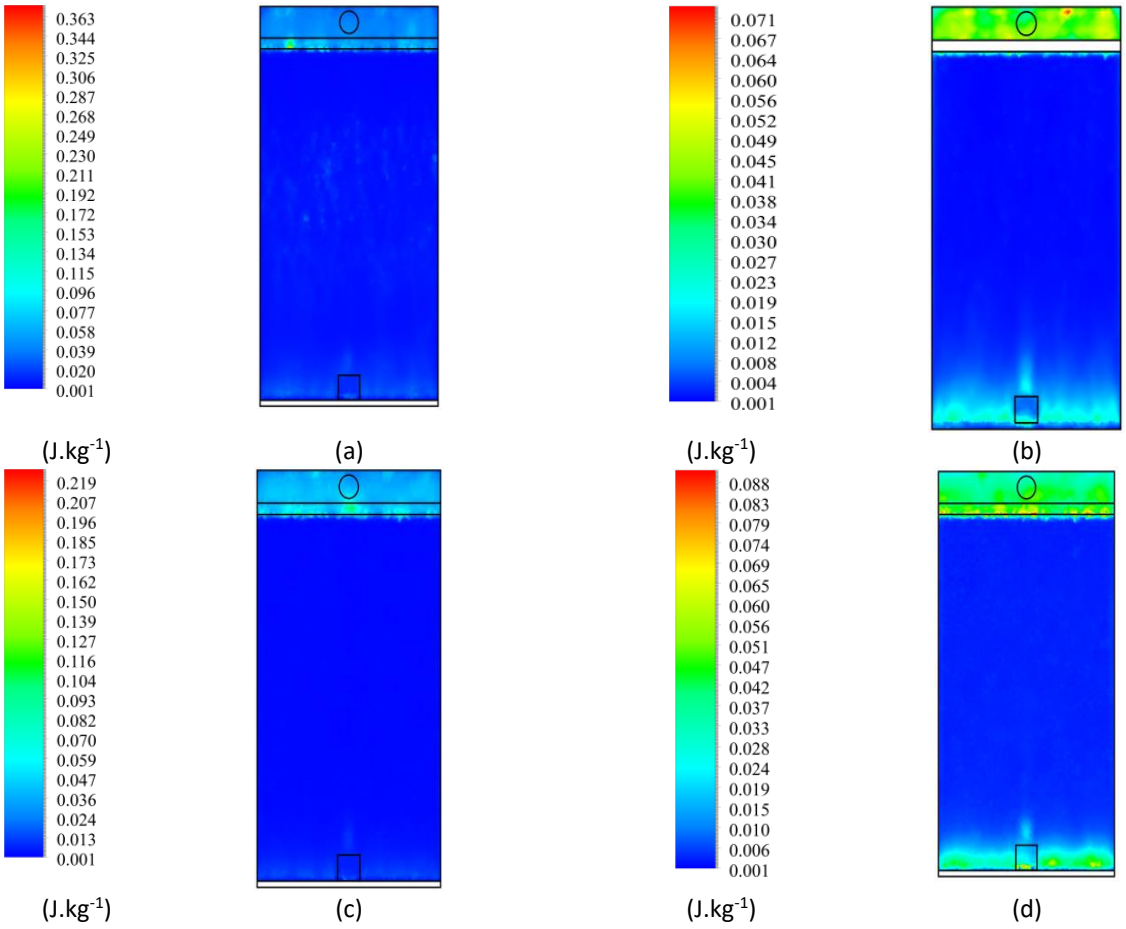

Fig. 17. Turbulent kinetic energy distribution in the plane defined by z = 0.013 m (a) D_s = 5 cm (b) D_s = 10 cm (c) D_s = 15 cm (d) D_s = 20 cm

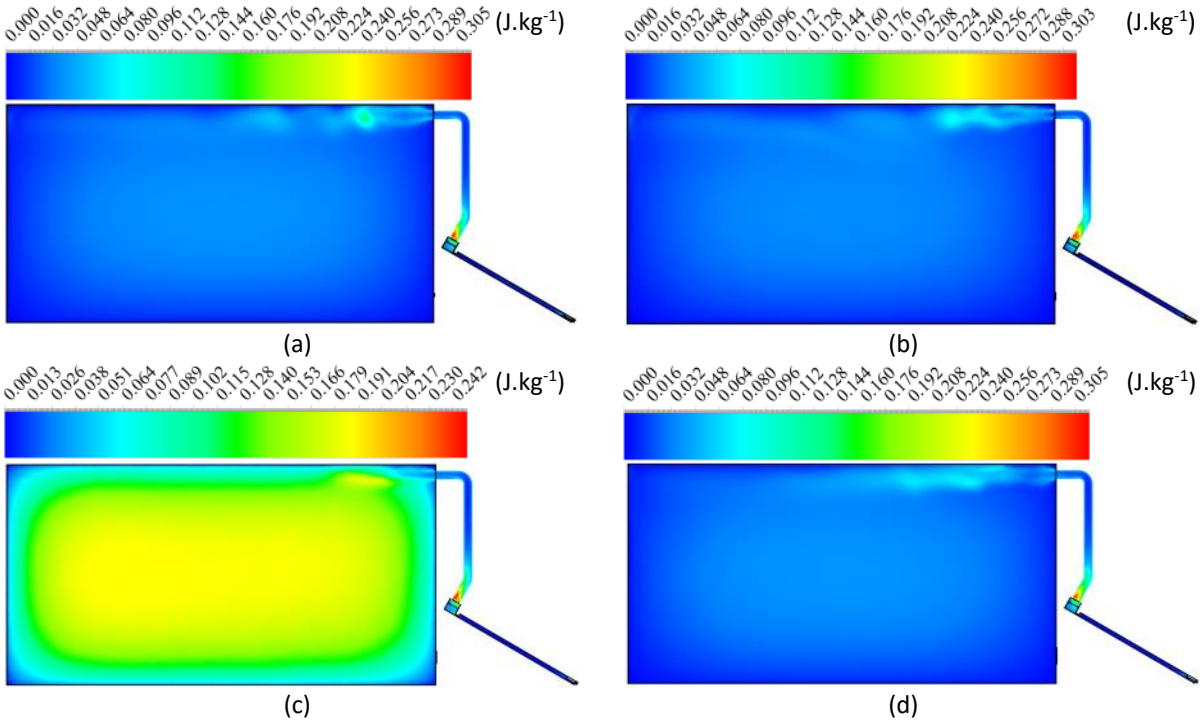

Fig. 18. Turbulent kinetic energy distribution in the plane defined by Y = 3.6 m (a) D_s = 5 cm (b) D_s = 10 cm (c) D_s = 15 cm (d) D_s = 20 cm

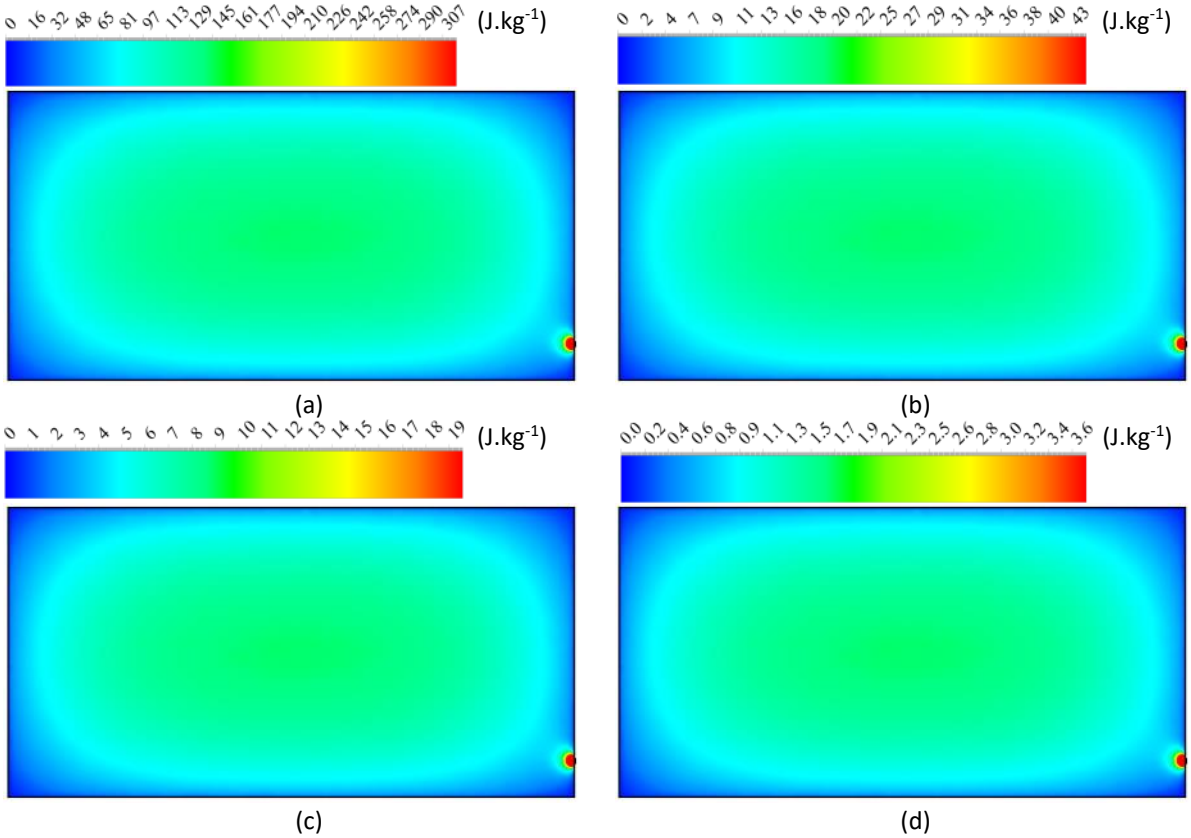

Fig. 19. Turbulent kinetic energy distribution in the plane defined by Y = 0.4 m (a) D_s = 5 cm (b) D_s = 10 cm (c) D_s= 15 cm (d) D_s = 20 cm

5.5 Dissipation Rate of the Turbulent Kinetic Energy

Figures 20, 21 and 22 show the distribution of the dissipation rate of the turbulent kinetic energy for the different representative planes defined by z = 0.013 m, Y = 0.4 m and Y = 3.6 m and for different diameters outlet diameters equal to D_s=5 cm, D_s=10 cm, D_s=15 cm, and D_s=20 cm. The wake zone characteristic of the maximum value of the dissipation rate of the turbulent kinetic energy appears is the same location. It appears in the collector air channel with an uniformity inside the panel air domain. However, the minimum values are located in the panel air volume in all over the planes. Inside the room, the dissipation rate of the turbulent kinetic energy distribution varies across the different geometrical system with a maximum value of ε= 51$m^2.s^{-3}$. The comparison between the results confirms that the maximum value of the dissiation rate of the turbulent kinetic energy is equal to ε= 51 $m^2.s^{-3}$ for the configuration defined by D_s= 5. However, the minimum value of the dissipation rate of the turbulent kinetic energy is equal to ε= 4 $m^2.s^{-3}$ for the configuration defined by D_s=20 cm.

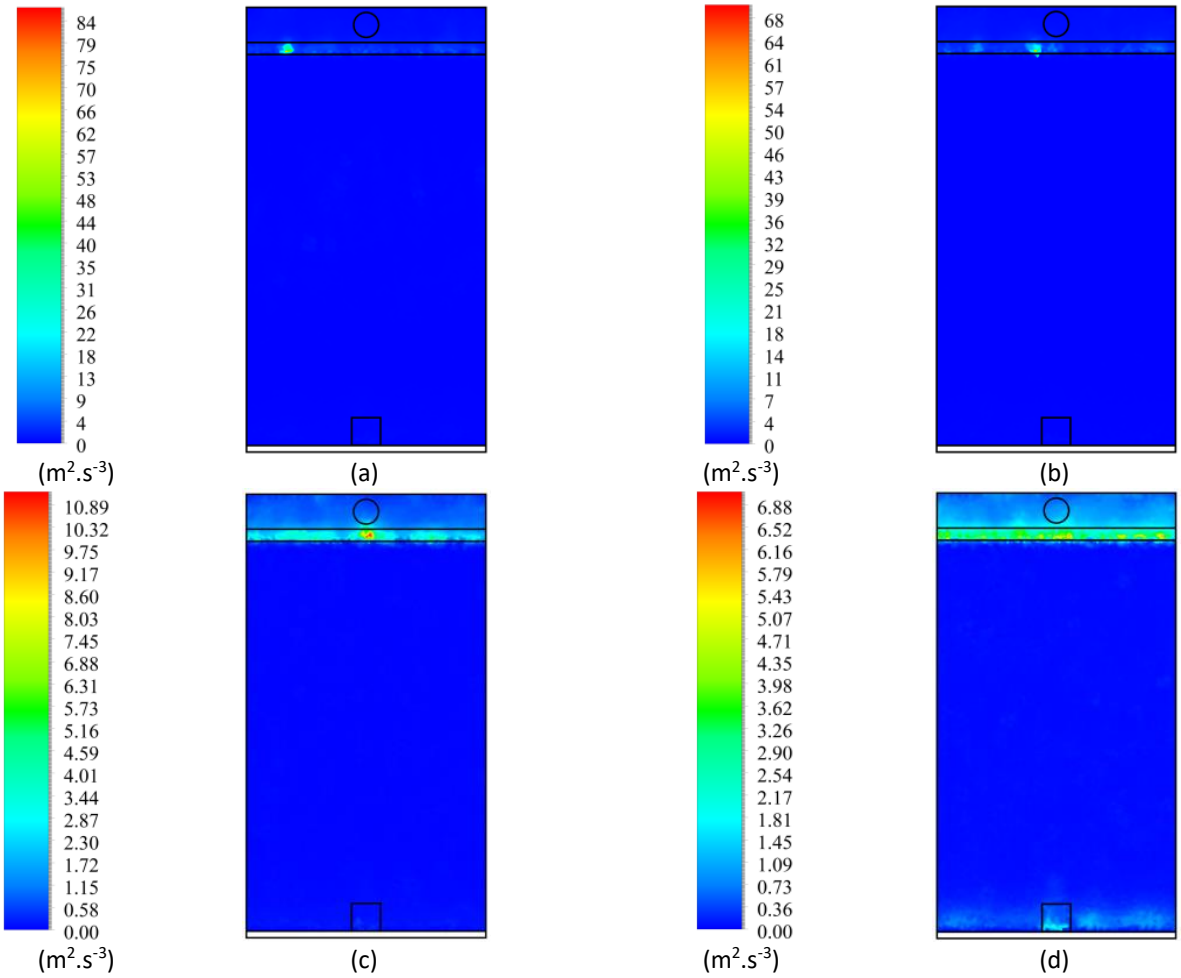

Fig. 20. Dissipation rate of the turbulent kinetic energy distribution in the plane defined by z = 0.013 m (a) D_s = 5 cm (b) D_s = 10 cm (c) D_s = 15 cm (d) D_s = 20 cm

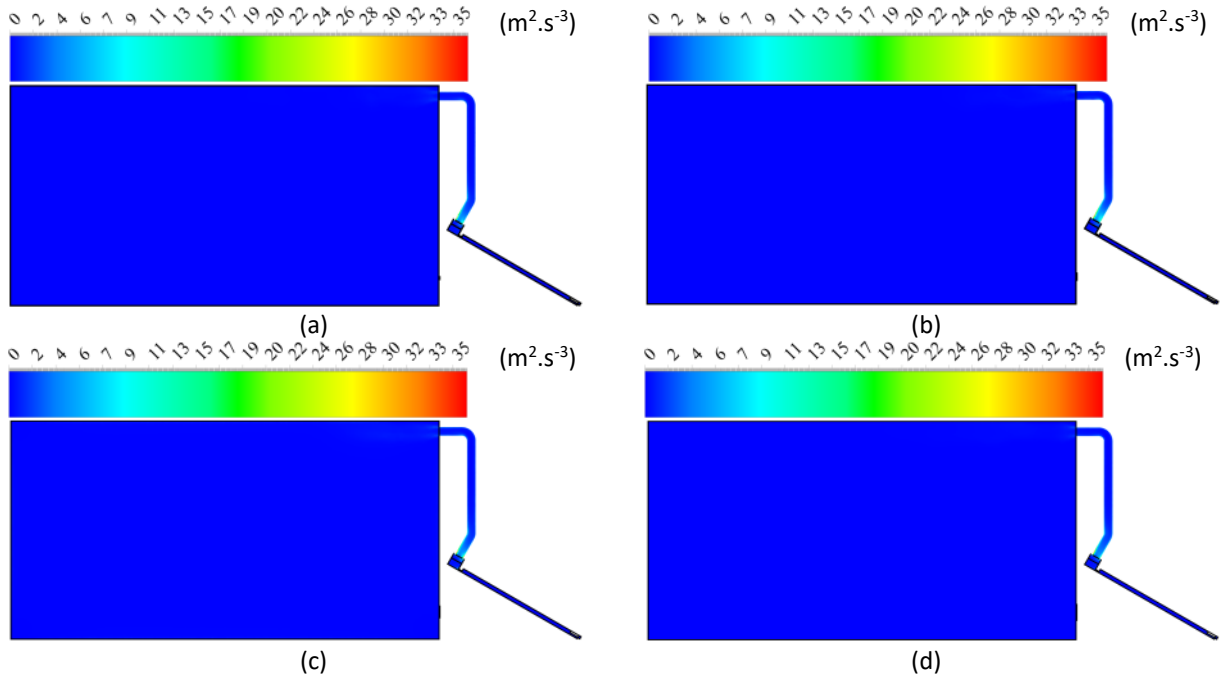

Fig. 21. Dissipation rate of the turbulent kinetic energy in the plane defined by Y = 3.6 m (a) D_s = 5 cm (b) D_s = 10 cm (c) D_s = 15 cm (d) D_s = 20 cm

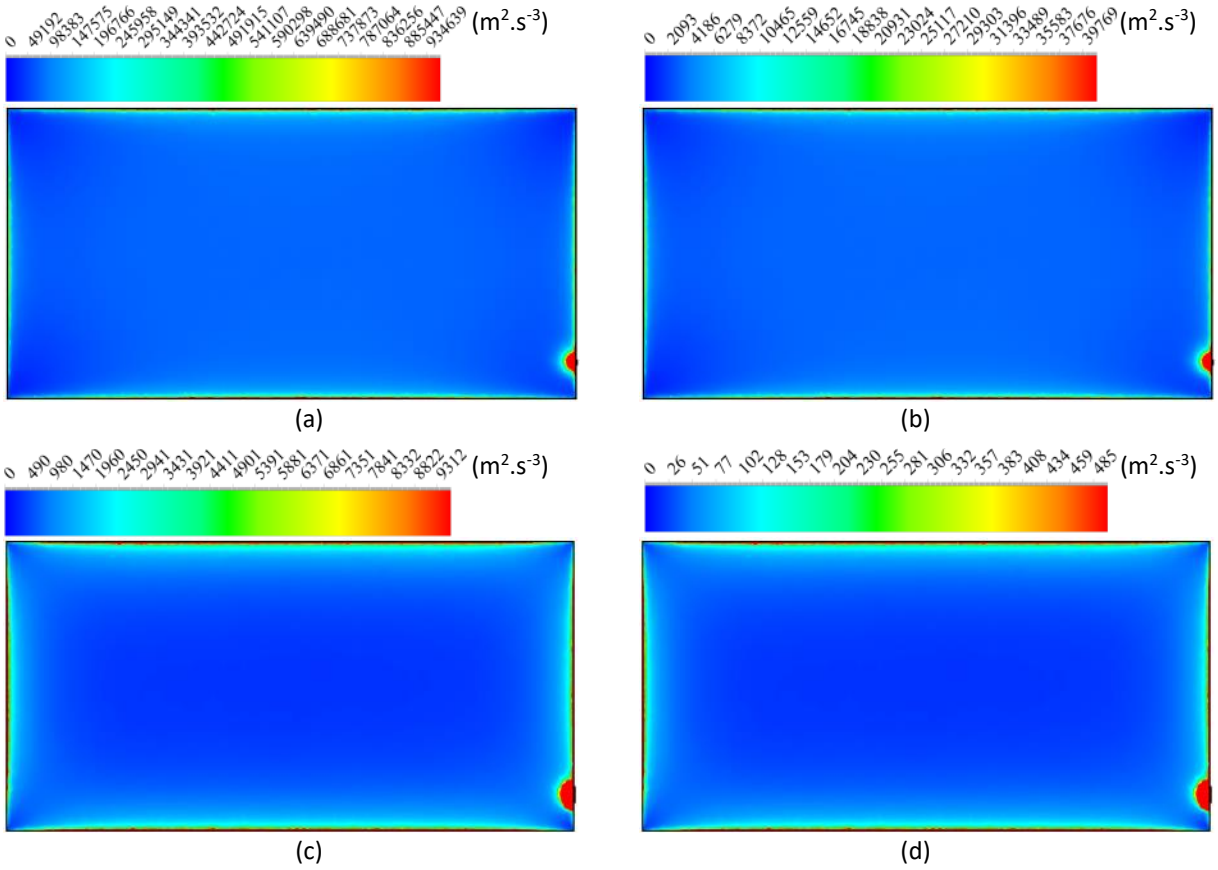

Fig. 22. Dissipation rate of the turbulent kinetic energy in the plane defined by Y = 0.4 m (a) D_s = 5 cm (b) D_s = 10 cm (c) D_s = 15 cm (d) D_s = 20 cm (a) D_s = 5 cm (b) D_s = 10 cm (c) D_s = 15 cm (d) D_s = 20 cm

5.6 Turbulent Viscosity

The distribution of the turbulent viscosity in the geometry air domain is depicted in Figure 23, 24 and 25 for the considered planes defined by z = 0.013 m, Y = 0.4 m and Y = 3.6 m and for different diameters outlet equal to D_s=5 cm, D_s=10 cm, Ds=15 cm, and D_s=20 cm. These planes defined by z = 0.013 m, Y = 0.4 m and Y = 3.6 m have been considered. From these results, the wake zone characteristic of the maximum value of the turbulent viscosity appears in the air channel with a uniformity inside the panel air domain. The minimum values are located in the panel air volume and it is equal to μ_t= 0.03 kg.m^{-1}s^{-1}. The maximum value of the turbulent viscosity reaches μ_t= 0.19 kg.m^{-1}s^{-1} in the first plane. Inside the room, the turbulent viscosity distribution varies across the different geometrical system with a maximum value of μ_t = 0.19 kg.m^{-1}.s^{-1}. The comparison between the results confirms that the maximum value of the turbulent viscosity is equal to μ_t = 0.19 kg.m^{-1}.s^{-1} for the configuration defined by D_s = 5c m. However, the minimum value of the turbulent viscosity is equal to μ_t = 0.03 kg.m^{-1}.s^{-1} for the configuration defined by Ds=20 cm.

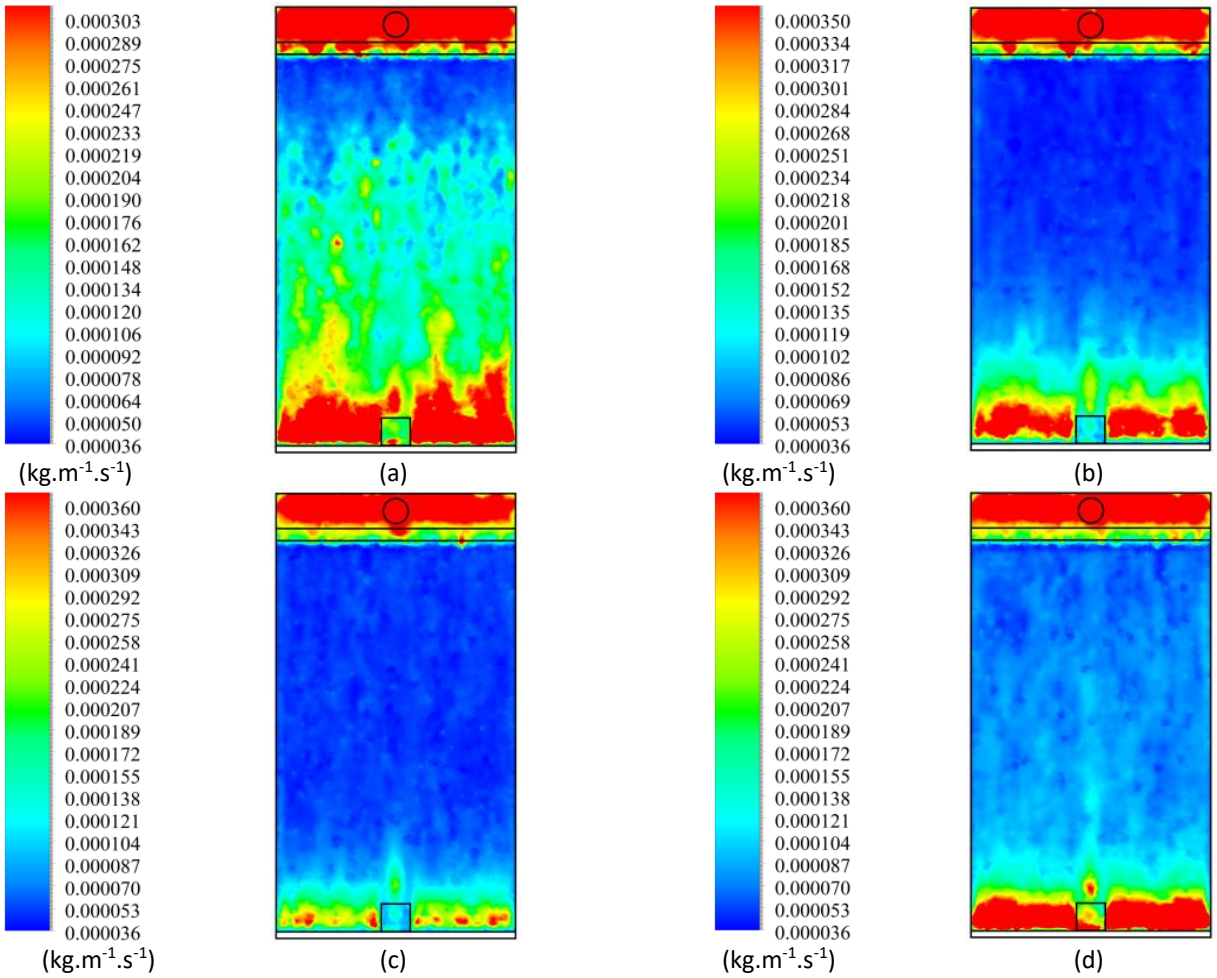

Fig. 23. Turbulent viscosity distribution in the plane defined by z = 0.013 m (a) D_s = 5 cm (b) D_s = 10 cm (c) D_s = 15 cm (d) D_s = 20 cm

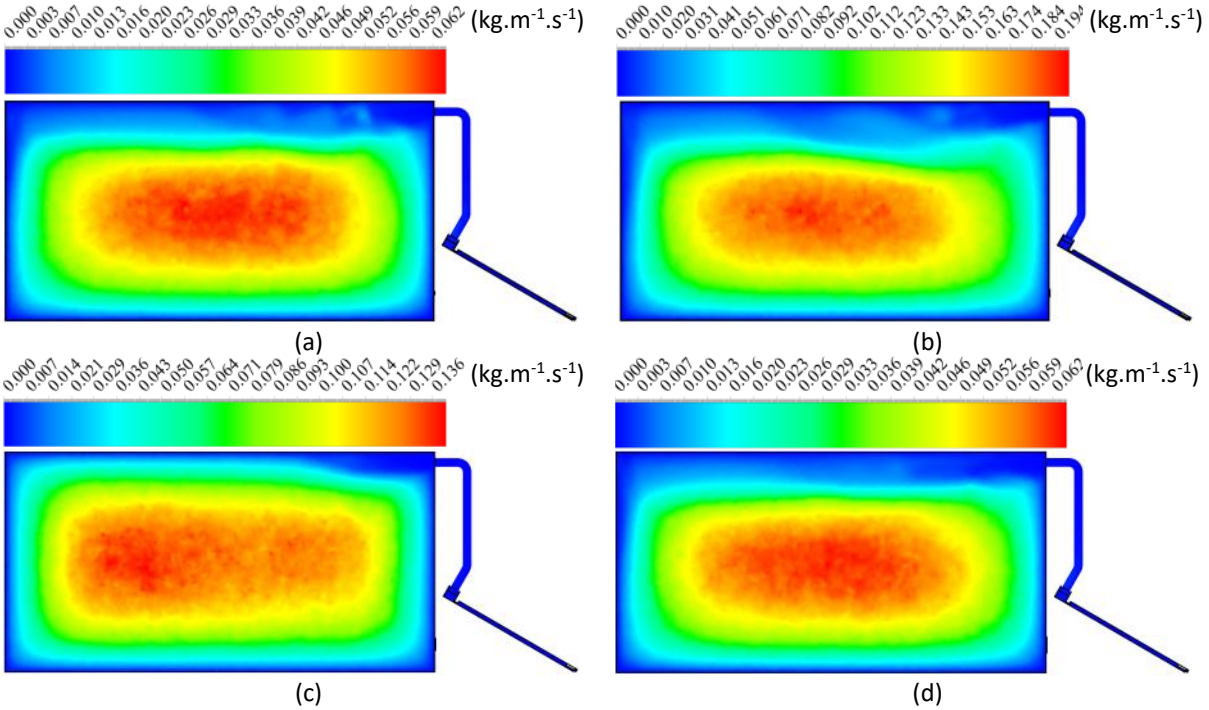

Fig. 24. Turbulent viscosity distribution in the plane defined by Y = 3.6 m (a) D_s = 5 cm (b) D_s = 10 cm (c) D_s = 15 cm (d) D_s = 20 cm

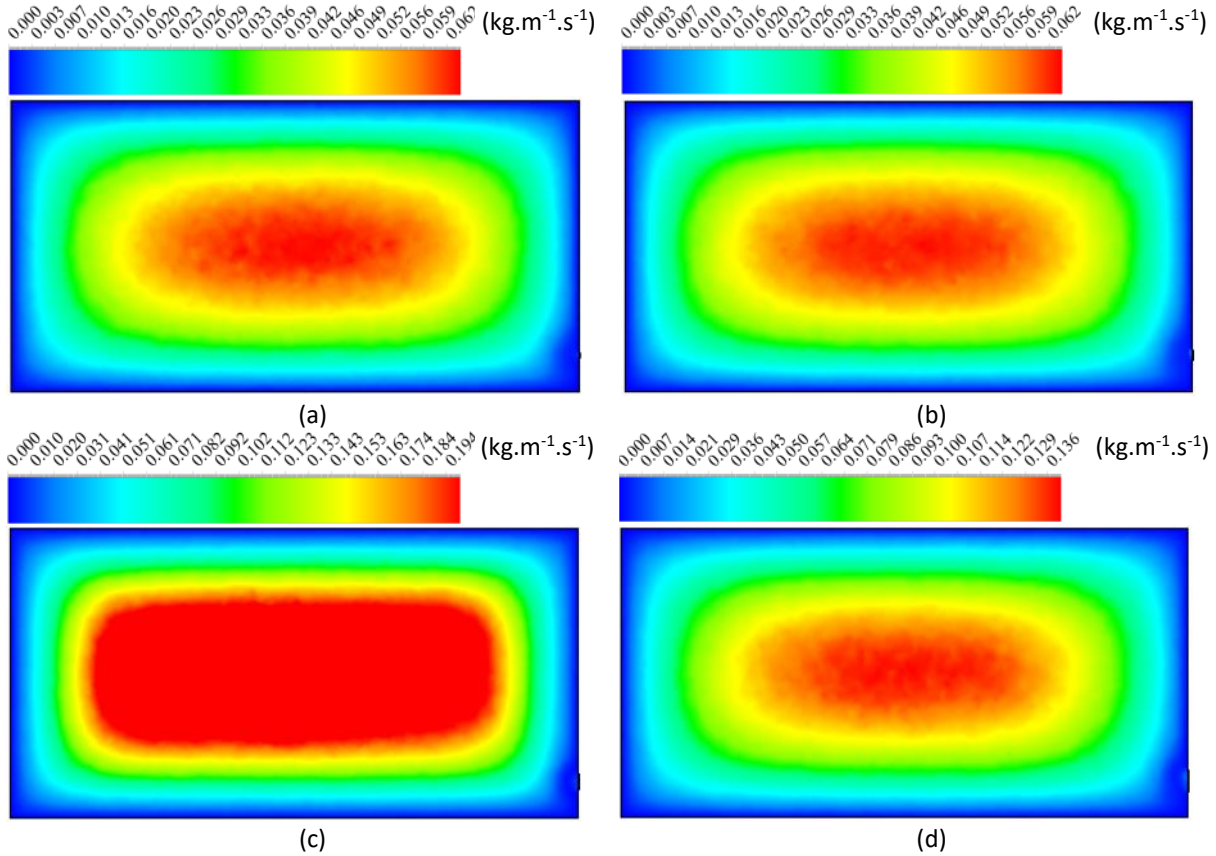

Fig. 25. Turbulent viscosity distribution in the plane defined by Y = 0.4 m (a) D_s = 5 cm (b) D_s = 10 cm (c) D_s = 15 cm (d) D_s = 20 cm

6. Conclusion

In this paper, we are interested in the study of the aerovoltaic solar air heater connected to a living room. This system is constituted by the integration of a closed channel under the photovoltaic panel to perform his electric performance and to produce the thermal energy to be used in the building requirements. To determine the effectiveness of using solar air heater in improving indoor air quality and thermal comfort, the connection between the room and the panel is set using a pipe that goes from the air-outlet of the panel through the wall of the room. To evaluate this new technique, we have developed numerical simulation inside the living room connected to the aerovoltaic solar air heater by using the numerical model software ANSYS Fluent. The numerical model was validated by the experimental data measured inside the aerovoltaic solar air heater. Our aims are to investigate the aerothermal structure inside a living room connected to an aerovoltaic solar air heaters to ensure the thermal comfort of the building. Following our numerical results, the collector presents a uniform distribution across the geometrical system with a temperature peak located just before the collector. Inside the room walls, it has been observed a uniformity in the temperature distribution with a maximum temperature at the connection point between the air pipe and the room wall. This temperature remains fixed until the air reaches the room and spreads inside the room space. The velocity distribution is uniform in the panel air domain. Inside the collector, an acceleration zone appears due to the complexity of the geometry. Inside the panel, the velocity presents the maximum value. Via the pipe separating the aerovoltaic panel from the room, a discharge area appears in the inlet hole and invaded the reverse wall. The static pressure distributions are not uniform under the panel. Inside the room, the static pressure distribution varies across the different geometrical system. Through the air advancement, the total pressure decreases

quietly in the expulsion area, produced from the air-inlet and through the room wall. By understanding the physics behind these factors, the non-uniform pressure distribution within the panel can be attributed to the intricate interplay of design elements, solar heat absorption, boundary conditions, and airflow characteristics. Analyzing these aspects provides valuable insights into optimizing the aerothermal structure for enhanced thermal comfort within the connected living room.

These outputs results will be used for the design and development of the building with a low energy consumption.

Acknowledgement
The Authors aim to acknowledge the Algerian and Tunisian Ministry of Higher Education and Scientific Research for financial support to the project LABEX N° AL 2 - N° TN 16.

REFERENCES

[1] Ojike, O., and W. I. Okonkwo. "Study of a passive solar air heater using palm oil and paraffin as storage media." *Case Studies in Thermal Engineering* 14 (2019): 100454.. https://doi.org/10.1016/j.csite.2019.100454

[2] Kumar, Sanjeev, Randip Kumar Das, and Kishor Kulkarni. "Comparative study of solar air heater (SAH) roughened with transverse ribs of NACA 0020 in forward and reverse direction." *Case Studies in Thermal Engineering* 34 (2022): 102015. https://doi.org/10.1016/j.csite.2022.102015

[3] Bazri, Shahab, Irfan Anjum Badruddin, Abdullah Yousuf Usmani, Saleem Anwar Khan, Sarfaraz Kamangar, Mohammad Sajad Naghavi, Abdul Rahman Mallah, and Ali H. Abdelrazek. "Thermal hysteresis analysis of finned-heat-pipe-assisted latent heat thermal energy storage application for solar water heater system." *Case Studies in Thermal Engineering* 40 (2022): 102490. https://doi.org/10.1016/j.csite.2022.102490.

[4] Gaonwe, Tsholofelo Priscilla, Kanzumba Kusakana, and Percy Andrew Hohne. "A review of solar and air-source renewable water heating systems, under the energy management scheme." *Energy Reports* 8 (2022): 1-10. https://doi.org/10.1016/j.egyr.2022.10.065

[5] Singh, Sarvapriya, Siddharth Suman, Santanu Mitra, and Manish Kumar. "Solar air heater with rotating circular ribs: Hybrid CFD-ANN approach for prediction of thermo-hydraulic performance." *Energy Reports* 8 (2022): 145-150. https://doi.org/10.1016/j.egyr.2022.10.084

[6] Jahangir, Mohammad Hossein, Arash Kargarzadeh, and Fatemeh Javanshir. "Energy investigation in buildings applying a solar adsorption chiller coupled with biofuel heaters and solar heating/cooling systems in different climates." *Energy Reports* 8 (2022): 15493-15510. https://doi.org/10.1016/j.egyr.2022.10.428

[7] Hassan, Ali, Ali M. Nikbahkt, Zachary Welsh, Prasad Yarlagadda, Sabrina Fawzia, and Azharul Karim. "Experimental and thermodynamic analysis of solar air dryer equipped with V-groove double pass collector: Techno-economic and exergetic measures." *Energy Conversion and Management: X* 16 (2022): 100296.. https://doi.org/10.1016/j.ecmx.2022.100296

[8] Guan, Jingxuan, Kailiang Huang, Jintian Xu, Guohui Feng, and Jiasen Song. "Performance of a collector-storage solar air heating system for building mechanical ventilation preheating in the cold area." *Energy and Built Environment* 4, no. 6 (2023): 639-652. https://doi.org/10.1016/j.enbenv.2022.06.003

[9] Gürel, Ali Etem, Gökhan Yıldız, Alper Ergün, and İlhan Ceylan. "Exergetic, economic and environmental analysis of temperature controlled solar air heater system." *Cleaner Engineering and Technology* 6 (2022): 100369. https://doi.org/10.1016/j.clet.2021.100369

[10] Al-Askaree, Ekram Hadi, and Nizar FO Al-Muhsen. "Experimental investigation on thermal performance of solar water heater equipped with Serpentine fin core heat exchanger." *Cleaner Engineering and Technology* 12 (2023): 100593. https://doi.org/10.1016/j.clet.2022.100593

[11] Markam, Bhupendra, and Subarna Maiti. "Artificial enhancer for small-scale solar air heater—a comprehensive review." *Cleaner Energy Systems* 4 (2023): 100046. https://doi.org/10.1016/j.cles.2022.100046

[12] Saxena, Abhishek, Nitin Agarwal, and Erdem Cuce. "Thermal performance evaluation of a solar air heater integrated with helical tubes carrying phase change material." *Journal of Energy Storage* 30 (2020): 101406. https://doi.org/10.1016/j.est.2020.101406.

[13] Shetty, Shreyas P., Akhil Paineni, Madhav Kande, N. Madhwesh, N. Yagnesh Sharma, and K. Vasudeva Karanth. "Experimental investigations on a cross flow solar air heater having perforated circular absorber plate for thermal performance augmentation." *Solar Energy* 197 (2020): 254-265. https://doi.org/10.1016/j.solener.2020.01.005.

[14] Yassien, Husam Naufal Saleh, Omar Rafae Alomar, and Mothana M. Mohamed Salih. "Performance analysis of triple-pass solar air heater system: Effects of adding a net of tubes below absorber surface." *Solar Energy* 207 (2020): 813-824. https://doi.org/10.1016/j.solener.2020.07.041
[15] Abdallah, Amr Sayed Hassan. "Passive air cooling system and solar water heater with Phase Change Material for low energy buildings in hot arid climate." *Energy and Buildings* 239 (2021): 110854. https://doi.org/10.1016/j.enbuild.2021.110854
[16] Zhu, Ting-ting, Yao-hua Zhao, Yan-hua Diao, Feng-Fei Li, and Zhen-hua Quan. "Experimental investigation and performance evaluation of a vacuum tube solar air collector based on micro heat pipe arrays." *Journal of cleaner production* 142 (2017): 3517-3526.http://dx.doi.org/10.1016/j.jclepro.2016.10.116
[17] Mazzucco, G., D. Muraro, V. Salomoni, C. Majorana, D. Marcuzzi, W. Rigato, P. Sonato *et al.,* "Structural analyses and integrated design of the MITICA Injector assembly." *Fusion Engineering and Design* 88, no. 6-8 (2013): 849-853. https://doi.org/10.1016/j.fusengdes.2013.01.078.
[18] Fellin, F., M. Boldrin, E. S. Cucinotta, and M. Zaupa. "Simulation and verification of air cooling system for-1MVdc MITICA High Voltage hall in Padova." *Fusion Engineering and Design* 146 (2019): 1069-1072. https://doi.org/10.1016/j.fusengdes.2019.02.007
[19] Ifa, Sondes, and Zied Driss. "Numerical simulation and experimental validation of the ventilation system performance in a heated room." *Air Quality, Atmosphere & Health* 14 (2021): 171-179. https://doi.org/10.1007/s11869-020-00923-6
[20] Bakri, Badis, Ahmed Ketata, Slah Driss, Hani Benguesmia, Zied Driss, and Fareh Hamrit. "Unsteady investigation of the heat ventilation in a box prototype." *International Journal of Thermal Sciences* 135 (2019): 285-297. https://doi.org/10.1016/j.ijthermalsci.2018.09.023
[21] Driss, Slah, Zied Driss, and Imen Kallel Kammoun. "Computational study and experimental validation of the heat ventilation in a living room with a solar patio system." *Energy and Buildings* 119 (2016): 28-40. http://dx.doi.org/10.1016/j.enbuild.2016.03.016
[22] Motte, Fabrice, Gilles Notton, Christian Cristofari, and Jean-Louis Canaletti. "Design and modelling of a new patented thermal solar collector with high building integration." *Applied energy* 102 (2013): 631-639. http://dx.doi.org/10.1016/j.apenergy.2012.08.012
[23] Miglioli, Alessandro, Niccolò Aste, Claudio Del Pero, and Fabrizio Leonforte. "Photovoltaic-thermal solar-assisted heat pump systems for building applications: Integration and design methods." *Energy and Built Environment* 4, no. 1 (2023): 39-56. https://doi.org/10.1016/j.enbenv.2021.07.002
[24] Ascione, Fabrizio, Martina Borrelli, Rosa Francesca De Masi, Filippo de Rossi, and Giuseppe Peter Vanoli. "A framework for NZEB design in Mediterranean climate: Design, building and set-up monitoring of a lab-small villa." *Solar Energy* 184 (2019): 11-29. https://doi.org/10.1016/j.solener.2019.03.083
[25] Borrallo-Jiménez, Milagrosa, Maria LopezDeAsiain, Paula M. Esquivias, and David Delgado-Trujillo. "Comparative study between the passive house standard in warm climates and nearly zero energy buildings under Spanish Technical Building Code in a dwelling design in Seville, Spain." *Energy and Buildings* 254 (2022): 111570. https://doi.org/10.1016/j.enbuild.2021.111570
[26] Cristofari, Christian, M. B. Carutasiu, Jean Louis Canaletti, R. Norvaišienė, Fabrice Motte, and Gilles Notton. "Building integration of solar thermal systems-example of a refurbishment of a church rectory." *Renewable Energy* 137 (2019): 67-81. https://doi.org/10.1016/j.renene.2018.05.026.
[27] Paraschiv, Spiru, Nicoleta Bărbuţă-Mişu, and Lizica Simona Paraschiv. "Technical and economic analysis of a solar air heating system integration in a residential building wall to increase energy efficiency by solar heat gain and thermal insulation." *Energy Reports* 6 (2020): 459-474. https://doi.org/10.1016/j.egyr.2020.09.024
[28] Fahmy, M., M. Morsy, H. Abd Elshakour, and A. M. Belal. "Effect of thermal insulation on building thermal comfort and energy consumption in Egypt." *Journal of Advanced Research in Applied Mechanics* 43, no. 1 (2018): 8-19.
[29] Alawi, Omer A., and Haslinda Mohamed Kamar. "Performance of Solar Thermal Collector Using Multi-Walled Carbon Nanotubes: Simulation Study." *Journal of Advanced Research in Micro and Nano Engineering* 2, no. 1 (2020): 12-21.
[30] Samsudin, Muhammad Syazwan Nizam, Md Mizanur Rahman, and Muhamad Azhari Wahid. "Sustainable power generation pathways in Malaysia: Development of long-range scenarios." *Journal of Advanced Research in Applied Mechanics* 24, no. 1 (2016): 22-38.